

Appendix XX

Subscale Ship Airwake Studies Using Novel Vortex Flow Devices with Smoke, Laser-Vapor-Screen and Particle Image Velocimetry

by

John E. Lamar (NASA-LaRC), Drew Landman (ODU), Russell S. Swift (ODU) and Paresh C. Parikh (NASA-LaRC)

ABSTRACT

Ships produce vortices and air-wakes while either underway or stationary in a wind. These flow fields can be detrimental to the conduction of air operations in that they can adversely impact the air vehicles and flight crews. There are potential solutions to these problems for both frigates/destroyers and carriers through the use of novel vortex flow or flow control devices. This appendix highlights several devices which may have application and points out that traditional wind-tunnel testing using smoke, laser-vapor screen, and Particle Image Velocimetry can be useful in sorting out the effectiveness of different devices.

1.0 INTRODUCTION

Ships at sea produce an air-wake that can be detrimental to air-operations. Figures 1-5 (from [1] to [3] & unpublished studies) show the problem notionally or computationally for a frigate and for carriers. The problems of chaotic flow behind a superstructure for a frigate/destroyer or separated bow flow and/or deck-edge flow for existing carriers are real. Since future ship architecture will have the same basic elements, one can expect the problems to be present on the next generation of surface craft (See carrier conceptual sketches in Figures 6-8 from [4] to [6]).

To alleviate these problems a variety of Novel Vortex Flow Devices (NVFD) or Flow Control Devices was suggested for a subscale ship air-wake study. They include a ramp, bow-flap, rounded bow, columnar vortex generator (CVG: [2], [7]), trapped vortex, and fence for the deck edges of carriers; and turning vanes, lateral wedges on top, angled plates, splitter plates, micro-vortex generators, passive porosity, pneumatics, and CVG for deckhouse corners. All are in need of study and some have been, such as the bow-flap on the LHA helicopter carrier [8]. Due to resource limitations, the CVG was selected for study due to its hypothesized [9] applicability to both carriers and frigates/destroyers (See Figures 9-13). Another reason for its selection is that not much is known about the actual capabilities of the device, hence some interesting results may occur. In order to provide an assessment of the CVG potential for impacting the air-wake, three experimental studies, supported by Navier-Stokes CFD solutions, were performed and form the basis of this appendix. [In addition to these CFD studies, Dr. Raj Nangia reports Euler solution results, beyond those of [7], obtained on a carrier model in Appendix XXI.] Among the experimental studies reported here, one is for the basic device alone and two are in combination with a helicopter-carrier ship model.

2.0 SYMBOLS

A,B,C Length of bow devices where ‘A’ is flush with the deck edges, ‘B’ is two inches wider, and ‘C’ is four inches wider and spans the entrance of the deck edge device

AOA	angle of attack, also α , in degrees
COBALT	Unstructured Navier-Stokes CFD flow solver (See http://www.cobaltcf.com/Codes/cobalt.htm – Accessed 09/28/05)
CFD	Computational Fluid Dynamics
CVG	Columnar Vortex Generator
d	diameter of CVG; really two times the maximum radius, inches; see Figure 14(c)
h	maximum height of plume centerline above the CVG, inches; see Figure 14(c)
LaRC	Langley Research Center (NASA)
LHA	‘A’ version of helicopter carrier (US Navy)
LHD	‘D’ version of helicopter carrier (US Navy)
LVS	laser-vapor-screen
NAVAIR	Naval Air Systems (US Navy)
NVFD	Novel Vortex Flow Devices
ODU-CEA	Old Dominion University-Center for Experimental Aeronautics
OML	Outer Mold Line
PIV	Particle Image Velocimetry
SBRT	Subsonic Basic Research Tunnel at NASA Langley Research Center
TsAGI	Central Aerohydrodynamic Institute
USM3D	Unstructured Navier-Stokes CFD flow solver (See http://ad-www.larc.nasa.gov/tsab/tetruss/ – Accessed 09/28/05)
WOD	Wind-over-deck, azimuth angle in degrees; positive nose left or = $-\Psi$
x	horizontal distance from downstream side of CVG to location of maximum plume height, inches; see Figure 14(c)
Θ	orientation angle associated with the opening of the CVG device, in degrees, where zero points directly upstream; positive clockwise
Ψ	model yaw angle, in degrees; positive nose right

3.0 FIRST SET OF TESTS

3.1 Experimental Test Purpose, Models, Setup, and Procedures

3.1.1 Purpose

The purpose of the test in the NASA Langley Subsonic Basic Research Tunnel (SBRT) was to obtain basic performance information for the CVG and the impact of changing various geometrical parameters. The results were measured in terms of height of the vortex system, as signified by the plume above the CVG, and the distance downstream at which this height occurs. Initial CVG application studies were also performed on a representative ship superstructure, a semi-span carrier bow region, and a low aspect-ratio rectangular wing.

3.1.2 Models

The primary models tested were nine basic CVGs. Regarding the CVGs, there were seven that had a Outer Mold Line (OML) radius of 2.00" at $\Theta = 0^\circ$ with an ending OML radius of 1.75", 1.625", 1.50", 1.00", 0.75", 0.50" and 0.50" at $\Theta = 360^\circ$. The two radii were connected by a helix. One of the last two CVGs had an additional spiral of 180° which ended with a radius of 0.25" at $\Theta = 540^\circ$. This last one was to ascertain whether a further spiraling would help to tighten the vortex, as had been suggested by CFD analysis shown later. The other two CVGs had an OML radius of 1.00" at $\Theta = 0^\circ$ with an ending OML radius of 0.75" and 0.50", respectively.

All CVGs models had the following characteristics: (1) made of Stereolithography (SLA) hardened resin; (2) wall thickness of 3/32"; (3) 4.0" diameter solid base of ~0.25" thickness; (4) exposed height of 10.0"; (5) opened at the top; and (6) painted flat black to enhance contrast with the white propylene-glycol smoke (vapor).

Figure 14(a) shows a typical CVG model, i.e. the 2.0" to 0.25", mounted on the support system in the SBRT with flow-and-smoke off and on. Figure 14(b) provides a contrast of two CVGs which have as their only difference the ending radii or ending values of Θ , one at 360° and one at 540° . The (c) part of this figure shows the definitions of the plume and CVG 'diameter' parameters that are used to summarize the plume performance results in Figure 15.

The ship superstructure was modelled using a box and tested with and without CVGs. This was a very crude representation and did not include the forward part of the ship or even a reflection plane.

The carrier model represented the forward-port quarter of a helicopter carrier, was made of foam board, had an overhang of the flight deck ahead of the hull, and was tested with and without CVGs. Figure 16 shows this model in the SBRT with and without smoke flow.

An alternate model test was also performed using a **horizontally mounted, flow-through device**, based on the CVG spiral, to assess whether it could control the strong side-edge vortex known to emanate off an aspect ratio 0.5 rectangular wing [10], i.e., just the support system. This device was developed by cutting off the base of the 2.0" to 0.5" CVG that was then mounted flush with the leading edge along the port side having the open slot pointed downward/inward (See Figure 17). The first application was to mount the maximum radius OML of the device to the **top** surface — designated upper for $\alpha > 0^\circ$ but lower for $\alpha < 0^\circ$ — along the first ten inches of the port edge. In this location, the device did extend laterally somewhat beyond the side edge with only a minimal amount of material being retained for securing the device to the wing. For the

second application, the device was translated vertically and affixed to the **bottom** surface — designated lower for $\alpha > 0^\circ$ but upper for $\alpha < 0^\circ$ — so that now the inner part of the maximum radius was flush with that surface. This placement was thought to better represent the carrier flight deck application due to the device not being attached to the surface from which the side-edge vortex would originate at $\alpha < 0^\circ$.

3.1.3 Setup

The basic support system consisted of **two** aluminium flat plates with dimensions of 12” wide by 24” long [aspect ratio 0.5] by 1/4” thick mounted onto the yaw sting in the SBRT using a 1.0” square aluminium block offset. The arrangement allowed the support plates – with side-edges parallel to the free-stream – and the CVG models to only have motion in the pitch plane along the tunnel center-line. The top plate had a 4.0” diameter hole with its center 14” behind the leading-edge along the center-line. The two plates were connected by two-sets of three, evenly-spaced, cap-head screws mounted along the sides from the bottom surface that went into top-plate threaded holes without protruding into the flow. The bottom plate had four circular slots in it, located underneath the hole, which allowed the mounted CVG to be affixed at angles ranging from 350° to 10° , or $\Theta = \pm 10^\circ$. This range of variation had been suggested based on the CFD simulations reported in reference 7. The CVGs were located in the top plate hole and affixed to the bottom plate with cap screws that went into four threaded holes in the CVGs bases. Neither the CVG base nor the screw threads protruded into the airstream. The flat plates were cut such that there was a 45° bevel made from the top plate to the bottom plate at the leading-edge, so that the bottom plate ended up slightly shorter than the top. Plate trailing-edges and sides were squared off; and, for photographic purposes, the top plate and left side-edges of both plates were painted flat-black to reduce glare.

The carrier model representation was mounted on a 1” by 2” by 36” support board with staples and the board affixed to the flat plate support system by double-back tape in the front and a C-clamp in the rear. A floor-to-ceiling reflection plane was used along the plane of symmetry for some runs but is not shown in Figure 16. This figure shows the model and tufted sidewall through the viewing window.

3.1.4 Procedures

All runs were made at very low dynamic pressure, mostly at a value 0.25 lbs/ft^2 and with the largest test value being 7 lbs/ft^2 , due to both tunnel and smoke visualization limitations. Video and still photos were taken of the smoke flow for later analysis. The CVGs were all tested at $\alpha = 0^\circ$ at various rotation angles ranging from 350° to 10° .

The ship superstructure was tested at $\alpha = 0^\circ$, whereas, the carrier model representation was tested with and without the vertical symmetry plane at various α 's, from 0° to 5° and at various dynamic pressures, ranging from 0.25 lbs/ft^2 to 5.0 lbs/ft^2 . The rectangular wing was tested over a range of α 's, from 10° to -10° and at $\alpha = -5^\circ$ over a range of dynamic pressures. Due to camera placement and with the top and one-side of the SBRT test section being clear, it was important to test at negative α 's so that the effects of the device could be visualized by the smoke flow.

3.1.5 Results

For the isolated CVGs there are some general observations: (1) the ones with the widest gap capture the most smoke – perhaps not surprising; (2) the wider the gap the more circulation

appears in the smoke patterns out the top of the CVG; (3) adding the additional 180° spiral helps to make the flow out of the CVG more coherent; and (4) there was almost always flow around both sides of the isolated CVG, so that the flow not captured yielded unsteady separated flow as for any circular cylinder.

Figure 15 provides a summary of the plume performance for all the CVGs. The better performers are those that have large values of h/d at the large values of x/d . The CVGs that best meet this criterion are those that have the smaller values of CVG r_{inner}/r_{outer} or with an extra half helical turn, i.e., Θ ending value of 540°.

The ship superstructure representation and the resulting flow was particularly bad, in fact it was difficult to get the smoke flow to go over the top of the “box” from the sides with smoke introduced at the 3” height of the CVG. This effort was abandoned due to the lack of fidelity in modelling the actual problem.

Another model was a portion of the helicopter carrier representation (forward-port quarter) but it did not develop any noticeable vortex action along its deck edge over an α range from 0° to 5°. This was disappointing and led to the question as to the origination of the deck-edge vortex, which is addressed later.

Due to the lack of success in generating a port-edge vortex along the helicopter carrier flight-deck, it was decided to do an alternate model test with the aspect ratio 0.5 rectangular wing with the goal of entraining most of the side-edge vortical flow there and having little or no flow left over to impinge on the new ‘upper surface’. From the studies performed, see Figure 17, the plate at $\alpha = -5^\circ$ shows that most of the smoke went inside the modified CVG device, the desired result, but some did manage to go around the device and impinge on the ‘upper surface’.

One issue is clear, once an appropriate CVG is designed, the question still remains as to how to scale it for the application.

3.2 CFD Support

Figure 18 presents the local C_p results from a USM3D Navier-Stokes solution for a CVG attached to a flat plate; in particular, the values for the combination at low α . These data for the plate and modified CVG device indicate little impact on the flow, as they both have essentially the same value/color. From a study of the velocity magnitude through the device — not shown — the expected effects of viscosity to diminish the velocity slightly from that of the freestream were noted.

Figure 19 shows the USM3D Navier-Stokes solution for a CVG with a gap of 0.5 inches at the SBRT test conditions. Figure 19(a) shows the geometry and flow direction, Figure 19(b) reports the local C_p distribution around the CVG and Figure 19(c) displays the Mach number values inside and outside of the CVG.

3.3 Concluding Remarks

From the experimental studies it has been learned that the: (1) widest gap in the CVG captures more smoke and apparently yields more initial circulation; (2) addition of the 180° internal spiral is also beneficial; and (3) not all the smoke flow is captured by the CVG as some passes on either side of the device. Both the experimental and computational studies show that the circulation gets reduced downstream of its creation, hence its persistence is limited.

4.0 SECOND SET OF TESTS -- LASER-VAPOR-SCREEN (LVS) TEST OF CVGS AND OTHER DEVICES ON LHD SHIP MODEL IN 14 FT BY 22 FT WIND-TUNNEL

4.1 Basic Helicopter Carrier Model

The basic helicopter carrier model was loaned by NASA Ames Research Center to LaRC as a courtesy. Ames has been performing wind-tunnel tests of helicopter and tilt-rotor aircraft on carriers for some time in order to understand the flow-fields and the associated interactions (See selected references [11] to [13]). Most of the carrier models studied experimentally at Ames in their 7 ft by 10 ft subsonic wind-tunnel are 1/48th scaled and, though simplified in terms of top-side features still, provide a solid basis for Particle Image Velocimetry (PIV) and other instrumented studies. In their cadre of ship models, there existed a 1/120th scaled model that had been constructed for other studies, but not yet tested. It was this model, capable of simulating either the LHA or LHD carrier, that was loaned to LaRC. Figure 20 shows the model in its 'as received condition' in the LHD configuration.

4.2 Modifications to Carrier Model

To prevent damage to the model and to provide mounting surfaces onto which devices could be affixed, the island was removed and another flight deck constructed – a glove – which slid over the original. The modified flight deck was 12.5 wide (0.5 inches wider), 80.25 inches long (0.25 inches longer at the bow), and 6.50 inches tall (0.50 inches taller). The island was reattached to the modified flight deck so that the distance between the island and the deck edge was maintained. Figure 21 shows the resulting model mounted in the 14 ft by 22 ft wind-tunnel.

4.3 Variety of CVGs and Other NVFD Tested

Figure 22 shows the variety of CVG and flap devices fabricated for test on the 1/120th scaled model. Three deck-edge devices (#2, #3, and #4) were variations of the CVG with different amounts of angular opening. There was also one CVG bow device (#6) that was designed to promote smooth on-flow to the flight deck at any Ψ , especially at 0° , and to aid the flow passing through the lower-curved portion to be captured by a deck-edge CVG for $\Psi \neq 0^\circ$. The bow flap (#5) was taken from previous studies [14] done at Ames as an example of one device showing flow improvement, and the trapped vortex device (#1) was constructed in two parts so that there could be the complete device (#1C or just #1) as well as the top only (#1A) and bottom only (#1B). Colleagues in the U.K. suggested the proportions for the deck-edge devices.

All these devices were constructed of 3/32nd inch thick SLA material. The deck-edge devices were made in 16.25 inch lengths (five in all/side) to facilitate fabrication and had a total length of 81.25 inches. This put the stern most part of the deck-edge behind the model when the forward portion was flush with the bow, but also allowed for a continuous deck-edge to be positioned ahead of the bow (1 inch) when the stern most part of the deck edge was flush with the stern.

The **bow devices** (#5 and #6) were made in **three lengths** of 12.5 inches, 14.5 inches and 16.5 inches and denoted 'A', 'B', and 'C', respectively. The 'A' length just covered the bow edge, whereas the four inch longer 'C' length was sufficient to cover the opening of the deck-edge device, and the 'B' length was halfway in-between. All three lengths were to be tested with the baseline model and as many of the deck-edge devices as possible.

question to be answered was the location of the deck-vortex origin $\Psi = 0^\circ$ on the baseline carrier. Figure 29 shows the LHA baseline model at $\Psi = 0^\circ$. From this figure, one can see that the vortex which wraps around the port deck-edge originates at the juncture of the flight-deck overhang with the hull. This was somewhat surprising and may be attributable to the cut-out at the flight-deck leading-edge for the LHA model. The expected origin was assumed to be at the juncture of the bow and deck edges, and may well be so for the LHD model which does not have this cut-out. Figure 30 shows the baseline LHA model at $\Psi = 30^\circ$ and the attendant vortex paths from the blunt bow and starboard deck edges, as well as the island.

Figures 31 and 32 show the LHA model with a bow flap at $\Psi = 0^\circ$ and 30° , respectively. The bow flap improves the overall flow with respect to the baseline at $\Psi = 0^\circ$ in that there is significant improvement over the flight deck up to where the island begins to have a strong influence. Some slight improvement in the flow at $\Psi = 30^\circ$ can also be inferred, but it is not as clear.

4.6.2 Simplified Baseline LHD carrier – NASA/ODU-CEA/USM3D

The LHD carrier was also examined and Figure 33 shows that the juncture of the bow and deck edges to be the source of the port deck vortex, as expected. Unfortunately, there are no streamlines available to help visualize the affect of the juncture of the flight-deck overhang with the hull on the deck edge vortex.

4.6.3 Euler Computations done in the U.K.

See [7] and Appendix XXI for other CFD studies done for a carrier with a CVG.

4.7 Acknowledgements

The authors gratefully acknowledge the help received from Ms. Gloria K. Yamauchi of NASA Ames Research Center who provided the ship model and the design suggestions made by Dr. Raj K. Nangia of Nangia Aero Research Associates (U.K.) and Dr. Doug Greenwell of Bristol University (U.K.) regarding the cross-sectional shapes of the novel vortex flow devices to be tested.

4.8 Concluding Remarks

The bow and deck edge devices make a difference in the flow around the carrier model by causing a change but, while encouraging, these results are only qualitative. Quantifiable results are needed in order to verify that what appear to be promising results from this study are actually real benefits. To that end a third set of tests was conducted on a subset of the devices reported here and is described in the next section. Moreover, Navier-Stokes solutions of the LHD carrier with CVG and/or other devices along the bow and deck-edges are needed for $\Psi \neq 0^\circ$.

5.0 THIRD SET OF TESTS -- PIV TEST OF CVGS AND OTHER DEVICES ON LHD SHIP MODEL IN ODU STUDENT TUNNEL [15]

5.1 Particle Image Velocimetry

PIV is a laser based flow diagnostic technique that has achieved recent popularity among fluid dynamics researchers. The benefits include a non-intrusive direct measurement of a velocity field in a fluid over a wide speed range from 1 meter/sec up to supersonic velocities. With successive measurements of velocity, vector maps, statistics, spatial correlations, and other relevant data are recovered. Both two and three velocity component versions of PIV systems are commercially

available. What follows is a brief description of the two component system used in the present study [16].

The fundamental hardware inherent to a PIV system includes the planar light source, scientific grade CCD camera, synchronizing electronics, flow seeder, and a computer with a “frame grabber” board. Typically a pair of lasers with cylindrical and spherical lenses are used to create a planar light sheet that can be pulsed twice in rapid succession. The laser light sheet is positioned over the region of interest and the camera is positioned normal to the sheet. A mineral oil flow seeder is used to inject micron sized particles into the flow field. The lasers are commanded to fire two bursts in rapid succession while the seed particle images are recorded in two frames by synchronizing the CCD camera. Velocity vectors are derived from sub-sections of the target area of the particle-seeded flow by measuring the movement of particles between the two light pulses. Once a sequence of two light pulses is recorded, the images are divided into small subsections called interrogation areas. The interrogation areas from each image frame, are cross-correlated with each other, pixel by pixel.

The correlation produces a signal peak, identifying the common particle displacement, Δx . A velocity vector map over the whole target area is obtained by repeating the cross-correlation for each interrogation area over the two image frames captured by the CCD camera. By knowing the time difference between pulses (Δt) and particle displacements (Δx), a direct calculation of the velocity may be computed as $\Delta x/\Delta t$. Repeating this process for each interrogation area yields the instantaneous velocity field. For a comprehensive discussion of the technique the reader is directed to reference 16.

The specifications for the Old Dominion University (ODU) Department of Aerospace Engineering PIV system are provided in Figure 34. The system is capable of resolving velocity vector fields at the rate of 3.75 measurements per second (hz). The physical size of the imaged light sheet is approximately 8.5 x 12 inches. The orientation of the PIV components for a centerline measurement on a carrier model is shown in Figure 35. Using the notation of the figure, in-plane velocity components u and w are measured using this configuration.

5.2 Experiment Overview

The use of CVG’s to control carrier deck edge separation was proposed. A wind tunnel experiment, using a 1/120th scaled LHD carrier was devised in order to evaluate device performance. Devices were placed along the bow leading edge, both alone and with devices on the (longitudinally oriented) side edges, as shown in

Run	Camera and Laser Setup	Model Configuration
1	Side Camera Longitudinal Centerline Laser Plane	Baseline, 0° Yaw
2		Bow CVG, 0° Yaw
3		Bow Flap, 0° Yaw
4	Side Camera Longitudinal Starboard Edge Laser Plane	Bow Flap, 0° Yaw
5		Bow Flap, 0° Yaw
6		Bow CVG, 0° Yaw
7		Baseline, 0° Yaw
8		Baseline, 20° Yaw
9		Bow Flap, 20° Yaw
10		Bow CVG, 20° Yaw
11	Side Camera Longitudinal Centerline Laser Plane	Bow and Side CVG’s, 20° Yaw
12		Side CVG, 20° Yaw
13		Side Flap, 20° Yaw
14		Bow and Side Flaps, 20° Yaw
15		Bow and Side Flaps, 20° Yaw
16		Baseline, 20° Yaw
17		Bow Flap, 20° Yaw
18		Side CVG, 20° Yaw
19		Bow and Side CVG, 20° Yaw
20		Bow CVG, 20° Yaw
21		Bow CVG, 0° Yaw
22	Rear Camera Lateral 10° from Bow Laser Plane	Baseline, 0° Yaw
23		Bow Flap, 0° Yaw

Table 2 Experimental PIV run matrix

Figure 25. It should be noted that the side edge devices only extended from the bow to a location 16.25 inches aft, as this was thought sufficient to capture the primary effect. The devices employed in this test were #5A and #6A for the bow, and #1A and #2 for the deck edge. The PIV system was used to measure instantaneous velocity fields and to gather statistics to assess turbulence and vorticity levels. Two dimensional velocity field measurements were made in a plane on the carrier deck centreline, in a plane parallel to the centreline but at the starboard deck edge, and in a lateral cross plane in the region of strong recirculation, 10 inches from the bow. A yaw angle was chosen to assess the sensitivity to cross winds, both a zero and 20 degree yaw were evaluated. The entire test matrix is provided in table 2.

For the centerline measurements (both at zero yaw and at 20 degrees yaw), the camera viewed the laser sheet through a window in the test section of the wind tunnel. The laser sheet was projected from a window above. For cross plane measurements the camera was moved to a downstream location in the flow and the laser assembly was rotated 90 degrees. The orientation of the model and the PIV system for both longitudinal and lateral velocity field measurements are shown in the schematics of Figure 36. PIV measurements at yaw were conducted by rotating the model, camera and laser 20 degrees to maintain the relative optical distances.

5.3 Experimental Details

5.3.1 Facility description

The Old Dominion University Low Speed Wind Tunnel (LSWT) is a closed return, fan driven, atmospheric pressure tunnel driven by a 125 horsepower electric motor. As shown in Figure 37, the tunnel has a unique dual test section design. The high-speed section measures 3 ft by 4 ft in cross section and is 8 feet long with maximum speeds of approximately 175 ft/sec. The low speed test section located upstream measures 7 ft by 8 ft in cross section, is 7 feet long, and has a maximum speed of approximately 37 ft/sec. The average freestream turbulence intensity measured in the high-speed test section is 0.2 %. Wind tunnel velocity is computed from differential pressure measurements across the tunnel contraction cone, temperature measurement in the high-speed test section from a thermocouple, and atmospheric pressure from a mercury barometer. All experimental Runs were conducted in the low-speed test section at a nominal velocity of 33 ft/sec.

A raised ground board with semicircular leading edge cross section was inserted in the low-speed test section so as to divide the flow in half. The model was then nominally positioned on the centerline of this ground board for the two yaw angles tested and is shown in the test section in Figure 38.

5.3.2 Deck-edge devices tested

Four devices were chosen for this study, two for the bow, and two for the longitudinal deck side edges. The bow CVG and flap along with the deck-edge CVG and flap are detailed in Figure 39. Only one of the five pieces of each deck-edge device was employed per model side, as explained previously.

5.4 Results and Discussion

The nature of this experiment was to evaluate the effectiveness of prototype devices in a more quantitative manner than was done previously in the 14 ft by 22 ft tunnel test. The ODU wind tunnel simulation was not perfect due to several key factors [17]. These include: (1) The blockage is rather high as the model is very large for the test section; (2) the Reynolds number is low in comparison to the full scale vehicle; (3) the model fidelity is rather crude; and (4) the atmospheric boundary layer was not simulated correctly. Despite the negation of these important

details, the experiment did capture the basic flow physics [8] and should serve as a foundation for further research and design work.

During this test, 100 image pairs were taken per Run at a rate of approximately 3.75 image pairs per second (hz). Statistical information was calculated over those 100 images. Non-lighted areas in the field of view of the camera were masked to blend in with the black background for clarity. It should be noted that spurious results from poor lighting conditions were removed from the average turbulence and vorticity plots.

A sample of the raw computed (mean) velocity vectors from Runs 1-3 is shown in Figure 40. These centerline velocity vector images immediately showed that both bow devices reduced leading edge separation and hence the downstream turbulence dramatically compared to the baseline case. The white dashed lines were added to show the approximate geometry of the test model. It should be noted that the starboard deck-edge laser plane location of Runs 4-7 provided little useful information due to the laser striking the visible side of the model and thus creating large regions that the PIV software couldn't evaluate properly – these Runs were omitted from the results. Runs 8-23 provided valuable turbulence results. The rear view raw vector images of Runs 15-23 showing low-magnitude cross flows and the effect of the side devices were not as revealing as their side view counterparts. The resulting raw vector images were more difficult to interpret directly and were omitted for brevity in favor of showing the turbulence results.

Node average turbulence is calculated by dividing the standard deviation of the velocity values from the 100 sample image pairs by the average velocity at each node. Results are presented as a percentage. Vorticity is calculated at each node using the following relation and is presented as a percentage:

$$vorticity = \frac{\left(\frac{\partial v}{\partial x}\right) - \left(\frac{\partial u}{\partial y}\right)}{2.0}$$

Comparing Figures 41, 42, and 43 (all at zero yaw) it is clear that both the bow devices significantly reduce the turbulence from well over 100% to well below 5% by eliminating the circulation bubble. The extent of the bubble will be exaggerated when these results are compared to full scale carriers due to the low Reynolds number [8]. The bow edge CVG appears to be equally effective at reducing turbulence when compared to the 22.5 degree bow flap. Figures 44-46 show that the plain bow flap (only) and bow CVG (only) reduce turbulence at the yawed condition, whereas the plain flap may be more effective. Figures 47 and 48 show that the bow CVG / side CVG and bow flap / side flap combinations reduce turbulence on the deck centerline at yaw to the magnitude seen in the zero yaw cases with only the bow devices in place. A side flap and side CVG (only) case was Run for completeness and showed (as expected) little effectiveness at yawed conditions. Figure 49 shows the deck centerline flow (side view) under the presence of the side CVG only at yaw.

Turning to the rear views, Figures 50-52 show the rear view of the deck with the starboard edge centered in the images. The baseline case (Figure 50) shows the large deck area affected by turbulence. Figures 51 and 52 reveal the powerful attenuation of turbulence provided by the bow devices. Figures 53 and 54 - rear view – show the benefit of employing bow and deck edge devices together in that the over-the-deck turbulence level is attenuated by a factor of approximately 20. In Figure 55 the rear view of the side CVG only is provided for completeness and shows no benefit when acting alone.

Vorticity calculations revealed similar information when compared to the turbulence calculations. In Figures 56 and 57, the effectiveness of the bow CVG may be seen. Comparing these Figures to 41 and 42 shows the same effected area over the deck. From a quantitative standpoint, the vorticity calculations confirm the turbulence level data already presented.

5.5 Conclusions of PIV Study

PIV measurements provided an excellent tool for evaluating the effectiveness of carrier deck-edge devices at reducing flight-deck turbulence. The resulting turbulence levels provided a clear picture of flow quality improvement in the plane of interest with no aerodynamic interference for the small number of devices tested. Moreover, the method and results were promising and these will prove useful in the future for investigating additional devices. Sample vorticity measurements corroborated well with the average turbulence measurements for the bow CVG.

The use of deck-edge devices in combination with bow-edge devices produced the best results in terms of lowering over-the-deck turbulence levels for the tested yaw angle of 20 degrees. The reduction in the turbulence level is on the order of a factor of 20. Both the CVG and the plain flaps proved effective when used on the bow and side edges. The bow-flap alone represents a good compromise in providing turbulence reduction with a very simple geometry. If these devices were to be considered for use on fleet aircraft carriers, it would most likely be more practical to add an angled bow flap than to create a curved surface around the entire deck edge.

It should be noted that these tests were conducted at Reynolds numbers much lower than the full-scale conditions. Referenced CFD, wind-tunnel and full scale tests have shown the same fundamental flow structures in the small scale model testing conducted here, but with the baseline full-scale patterns showing reattachment to occur more forward at zero yaw.

5.6 Acknowledgements

The authors gratefully acknowledge the help provided by Dr. Colin P. Britcher of ODU with the PIV system.

6.0 CONCLUDING REMARKS

Ships conducting air operations at sea produce vortices and wakes that can adversely affect air vehicles and flight crews. There are potential solutions to these problems for both frigates/destroyers and carriers through the use of Novel Vortex Flow or Flow Control Devices, some of which were investigated in this appendix. The primary devices examined herein are the Columnar Vortex Generator and the flap as applied to both the bow and deck edge of a simplified helicopter carrier model. From the laser-vapor screen studies of these devices on this model, changes were noted to occur over the flight-deck that were interpreted as flow improvements. However, it remained for the PIV studies to confirm that these devices produced the desired result of reducing the turbulence over the flight deck or making the flow-field there resemble an undisturbed free stream. Even though the PIV studies were restricted to the forward part of the carrier model, this is the region where adverse disturbances are generated that eventually propagate over the aft part of the flight deck. One problem not treated by these devices is that of the island wake. It can become a major player and needs to be addressed.

7.0 REFERENCES

- [1] Polsky, Susan A.; and Bruner, Christopher W.S.: *A Computational Study of Unsteady Ship Airwake*, In *Advanced Flow Management Symposia – Part A*. RTO-MP-69 Paper 25, Loen Norway, May 2001.
- [2] Lugt, Hans J.: *Vortex Flow in Nature and Technology*. John Wiley & Sons 1983, pp. 39, 143.
- [3] Maslov, L.A.; Valuev, N.O.; Zharinov, A.V.: *The experience of aerodynamic disturbances research behind an aircraft-carrier ship with elements for safe operation of ship-based aircraft*, In *Fluid Dynamics Problems of Vehicles Operating Near or in the Air-Sea Interface*. RTO MP-15, pp. 9-1 to 9-6, 1998.
- [4] Aviation Week & Space Technology, February 3, 2003, pp. 32-33.
- [5] <http://www.naval-technology.com/projects/cvf/cvf69.html>. Accessed 07/07/05.
- [6] Courtesy of Northrop Grumman Newport News Shipbuilding.
- [7] Nangia, Raj; and Lumsden, R.B.: *Novel Vortex Flow Devices - Columnar Vortex Generators Studies for Airwakes*. AIAA-2004-2348, presented at the AIAA 34th Fluid Dynamics Conference in Portland OR, June 28-July 1, 2004.
- [8] Czerwiec, Ryan; and Polsky, Susan A.: *LHA Airwake Wind Tunnel and CFD Comparison with and without Bow Flap*. AIAA paper AIAA-2004-4832, presented at the AIAA 22nd Applied Aerodynamics Conference and Exhibit in Providence RI, August 16-19, 2004.
- [9] Lamar, John E.: *Modifying Ship Air-Wake Vortices for Aircraft Operations*. NASA TechBrief, March 2004 (Invention Disclosure LAR 16281-1, 2001).
- [10] Lamar, John E.: *Extension of Leading-Edge-Suction Analogy to Wings with Separated Flow around the Side Edges at Subsonic Speeds*. NASA TR R-428, October 1974.
- [11] Wadcock, Alan J.; Yamauchi, Gloria K.; Heineck, James T.; Silva, Mark J.; and Long, Kurtis R.: *PIV Measurements of the Wake of a Tandem-Rotor Helicopter in Proximity to a Ship*. Presented at the AHS 4th Decennial Specialist's Conference on Aeromechanics, San Francisco, CA January 21-23, 2004.
- [12] Silva, Mark J.; Yamauchi, Gloria K.; Wadcock, Alan J.; and Long, Kurtis R.: *Wind-Tunnel Investigation of the Aerodynamic Interactions between Helicopters and Tiltrotors in a Shipboard Environment*. Presented at the AHS 4th Decennial Specialist's Conference on Aeromechanics, San Francisco, CA January 21-23, 2004.
- [13] Rajagopalan, Ganesh; Schaller, David; Wadcock, Alan J.; Yamauchi, Gloria K.; Heineck, James T.; and Silva, Mark J.: *Experimental and Computational Simulation of a Model Ship in a Wind Tunnel*. AIAA Paper No. 2005-1347, Presented at the AIAA 43rd AIAA Aerospace Sciences Meeting and Exhibit, Reno, NV, Jan. 10-13, 2005.
- [14] Long, Kurtis R.: Private communication, March 5, 2001.

- [15] Landman, Drew; Lamar, John E.; and Swift, Russell: *Particle Image Velocimetry Measurements to Evaluate the Effectiveness of Deck-Edge Columnar Vortex Generators on Aircraft Carriers*, In *AVT-124 Specialists' Meeting on "Recent Developments in Non-Intrusive Measurement Technology for Military Application on Model- and Full-Scale Vehicles"*. RTO-MP124 Paper #7, Budapest, Hungary, April 25-29, 2005.
- [16] Raffel, M., Willert, C., and Kompenhans, J.: *Particle Image Velocimetry*. Springer-Verlag, New York, 1998.
- [17] Barlow, J.B., Rae, W.H., and Pope, A.: *Low Speed Wind Tunnel Testing*. 3rd ed., John Wiley and Sons, 1999.

8.0 FIGURES

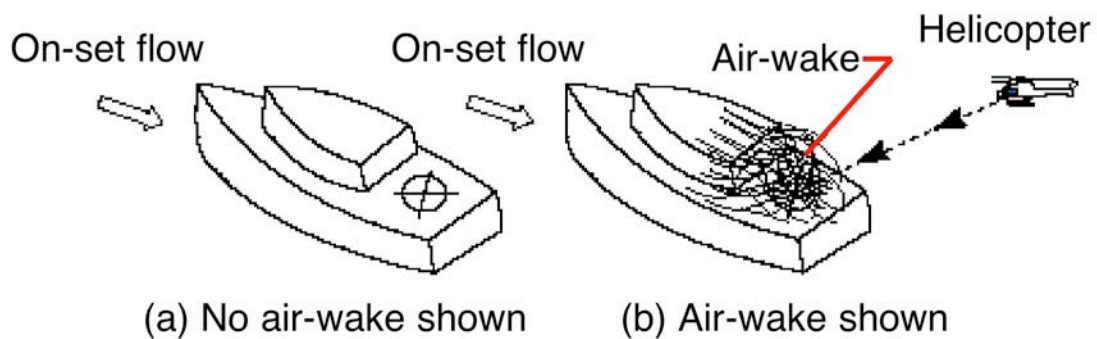


Figure 1. Air-wake problem due to frigate superstructure depicted.

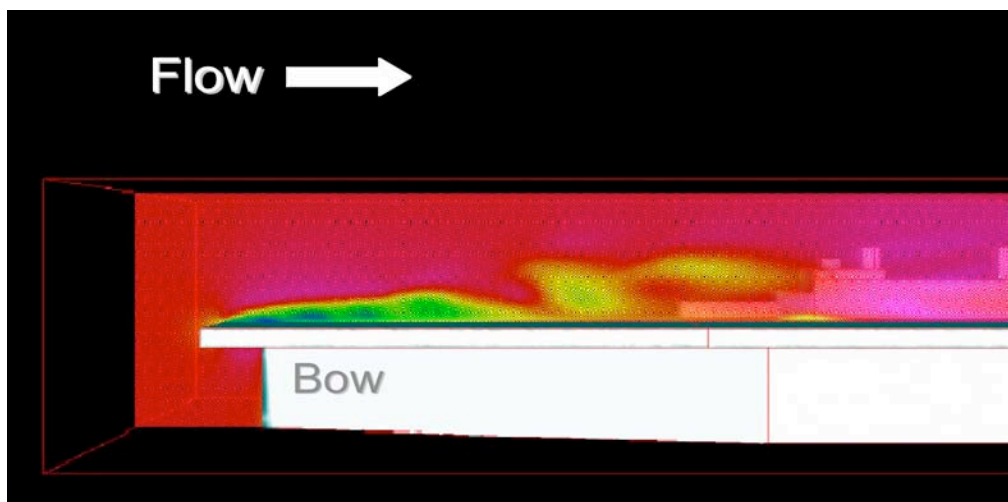


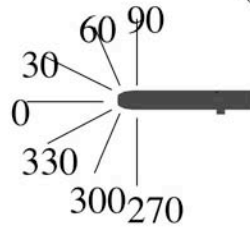
Figure 2. Centerline u-velocity component on LHD carrier model from NASA/ODU-CEA/USM3D study.



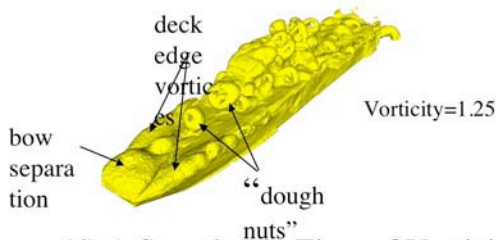
(a) LHA-2, the USS Saipan.



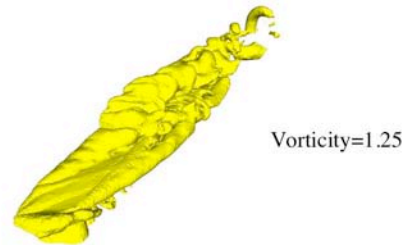
(b) CFD Model of an LHA



(c) Wind-over-deck azimuths



(d) A Snapshot in Time of Vorticity iso-surfaces for WOD=0°, 30kt



(e) A Snapshot in Time of Vorticity iso-surfaces for WOD=30°, 30kt

Figure 3. CFD model of on LHA helicopter carrier and NAVAIR/COBALT solutions at two WOD (-Yaw) angles [1].

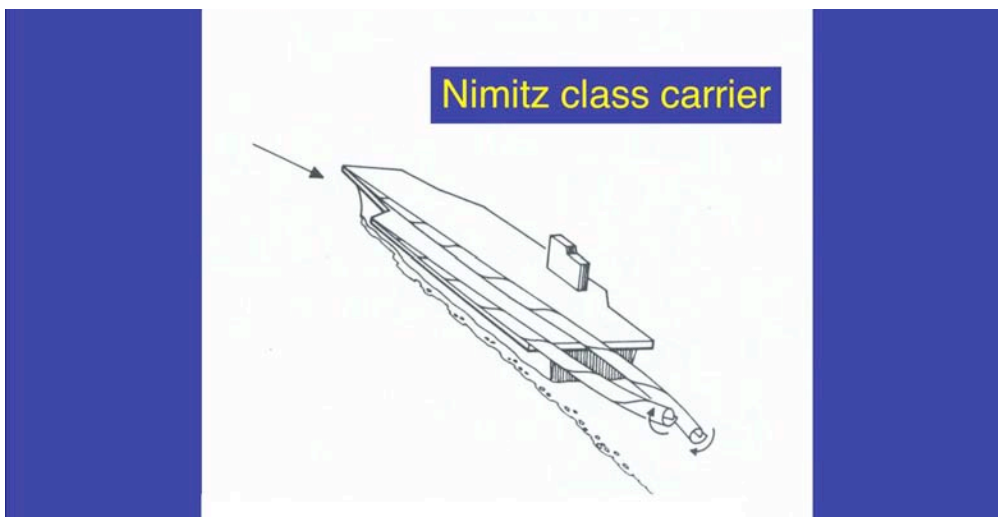


Figure 4. Air-wake depicted from Nimitz class aircraft carrier [2].

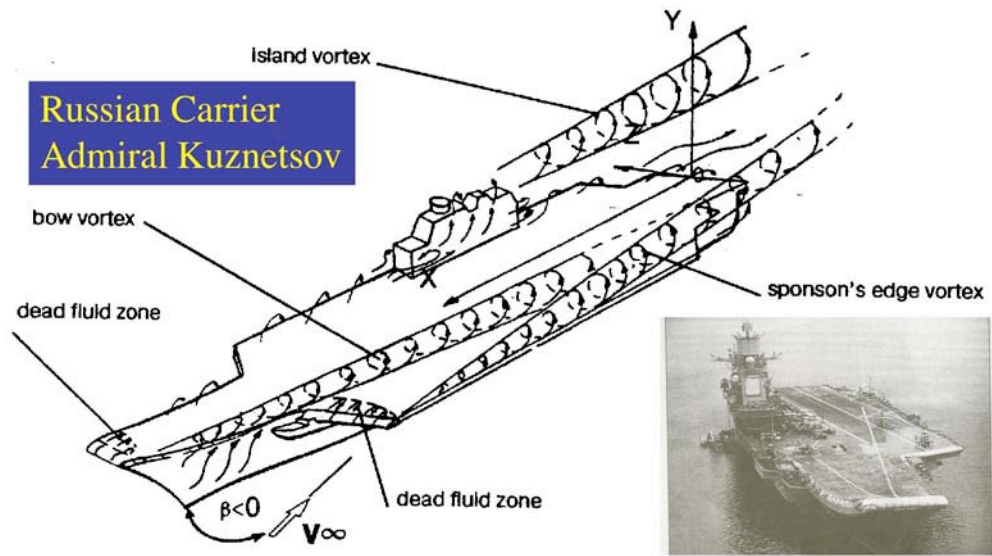


Figure 5. Air-wake off of Russian carrier Admiral Kuznetsov [3].



Figure 6. Proposed British aircraft carrier without [4] and with ski-jump.



Figure 7. Alternative British aircraft carrier with ski-jump [5].



Figure 8. Concept of CVN-21: Advanced US Carrier [6].

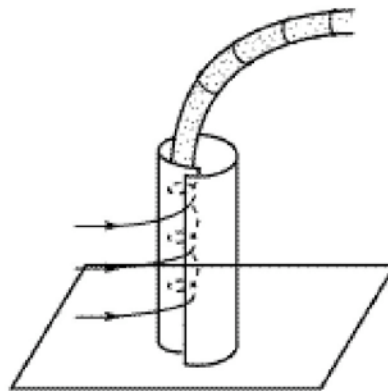


Figure 9. Columnar Vortex Generator (CVG) -- a potential novel vortex flow control device [2].

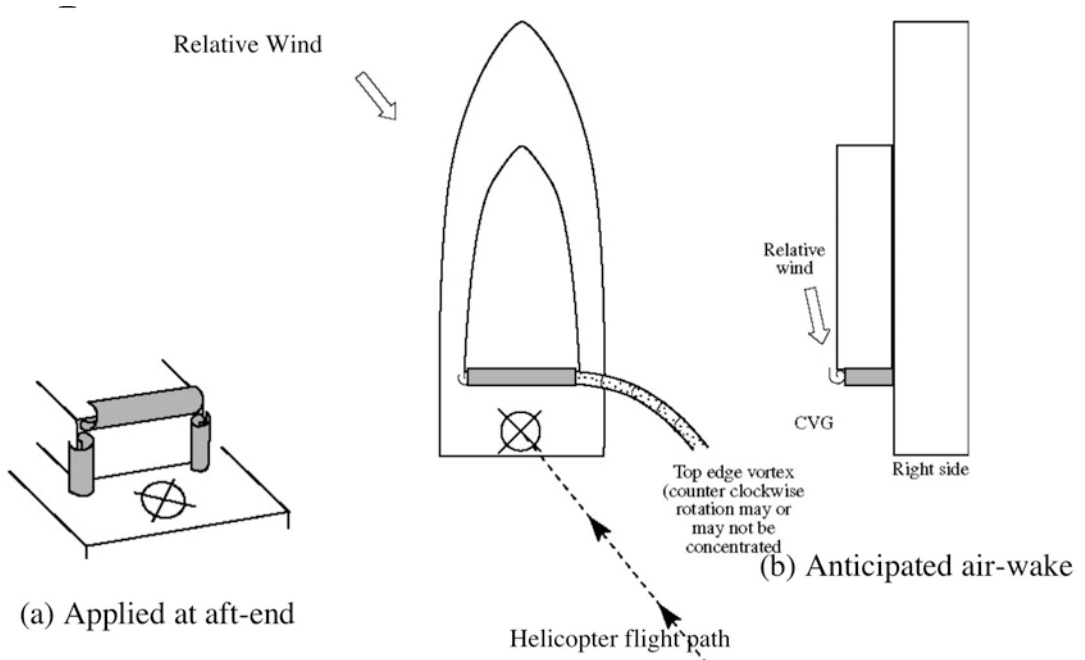


Figure 10. Potential CVG application to the superstructure air-wake problem.

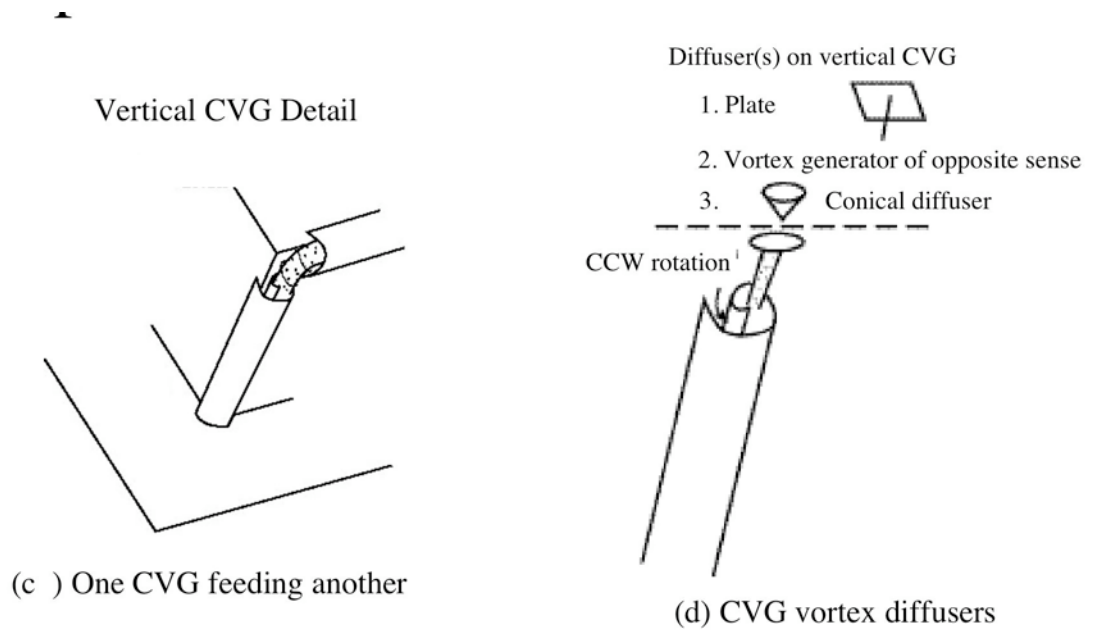


Figure 11. Details of CVG application to superstructure.

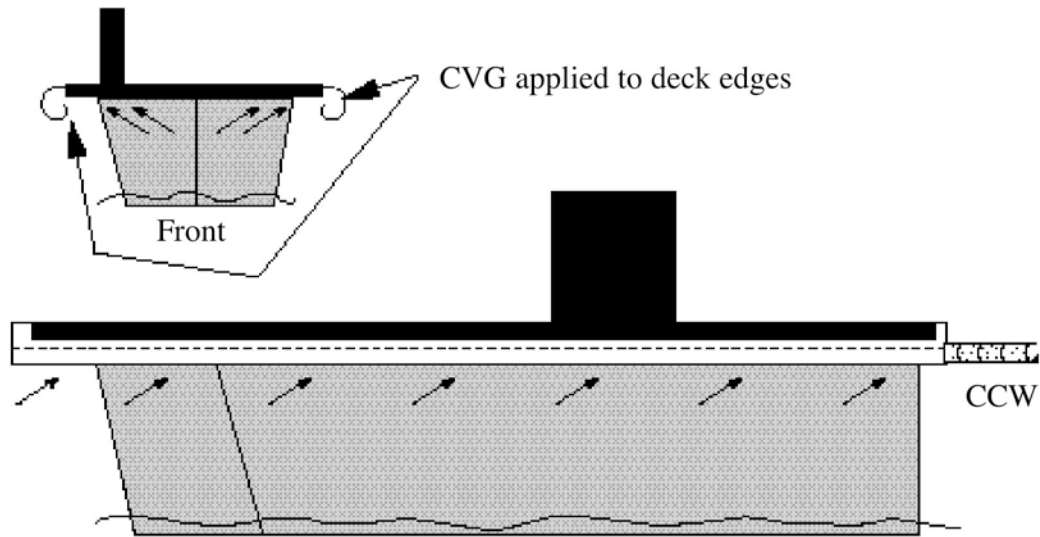


Figure 12. Potential CVG application to carrier deck-edge vortex problem; head-on and port views.

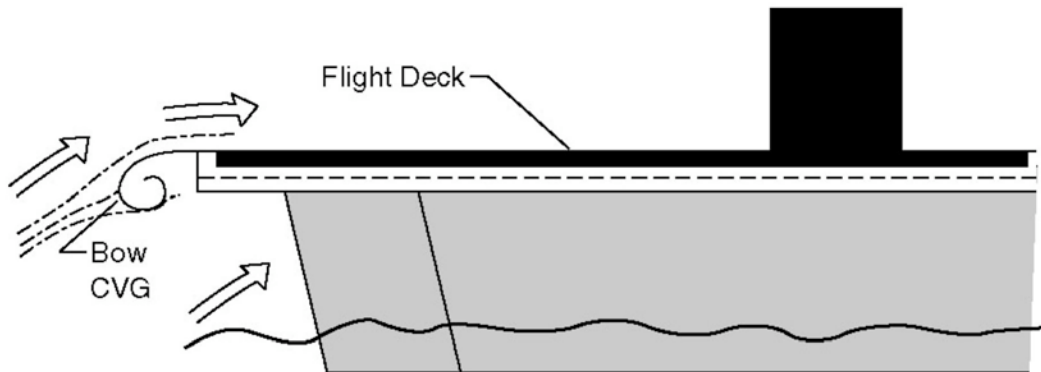
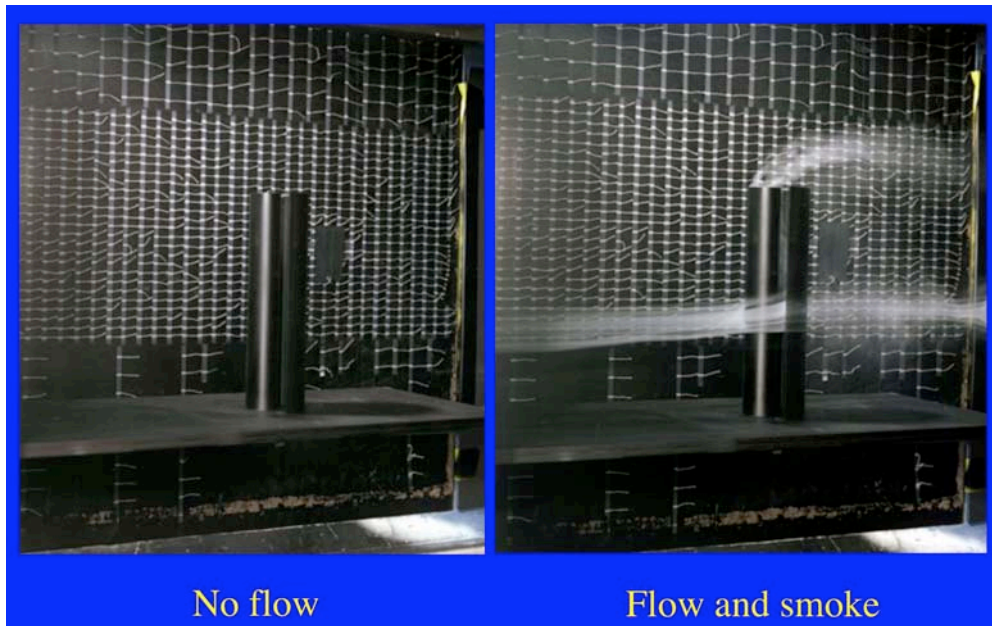
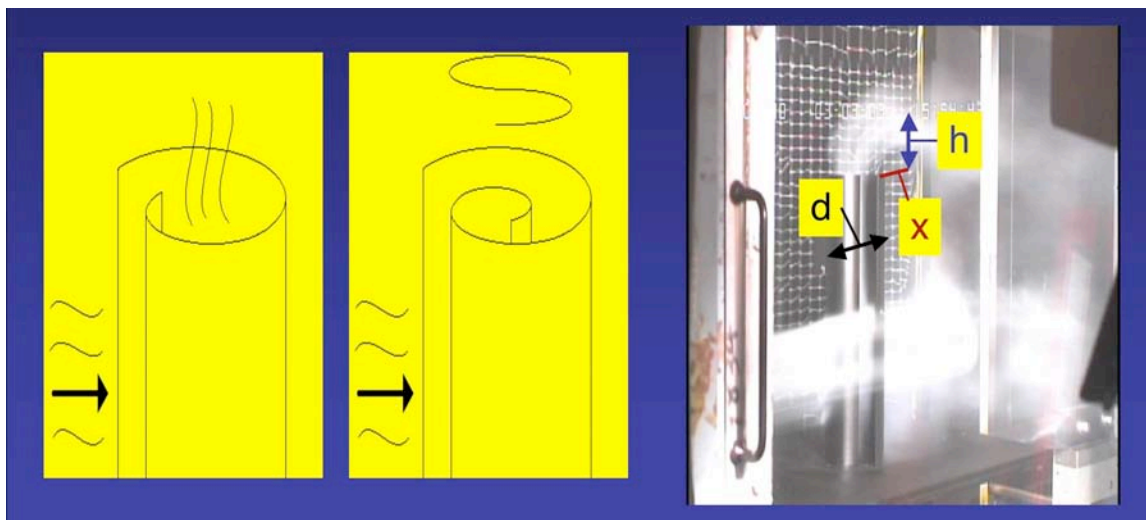


Figure 13. Potential CVG application to carrier bow vortex problem; port view.



(a)



(b)

(c)

Figure 14. Columnar Vortex Generator without and with smoke and pertinent geometry and plume parameters defined: (a) 2.0" to 0.25" CVG; (b) Two CVGs with different amount of helical coil; (c) LaRC SBRT smoke-flow pertinent parameters defined.

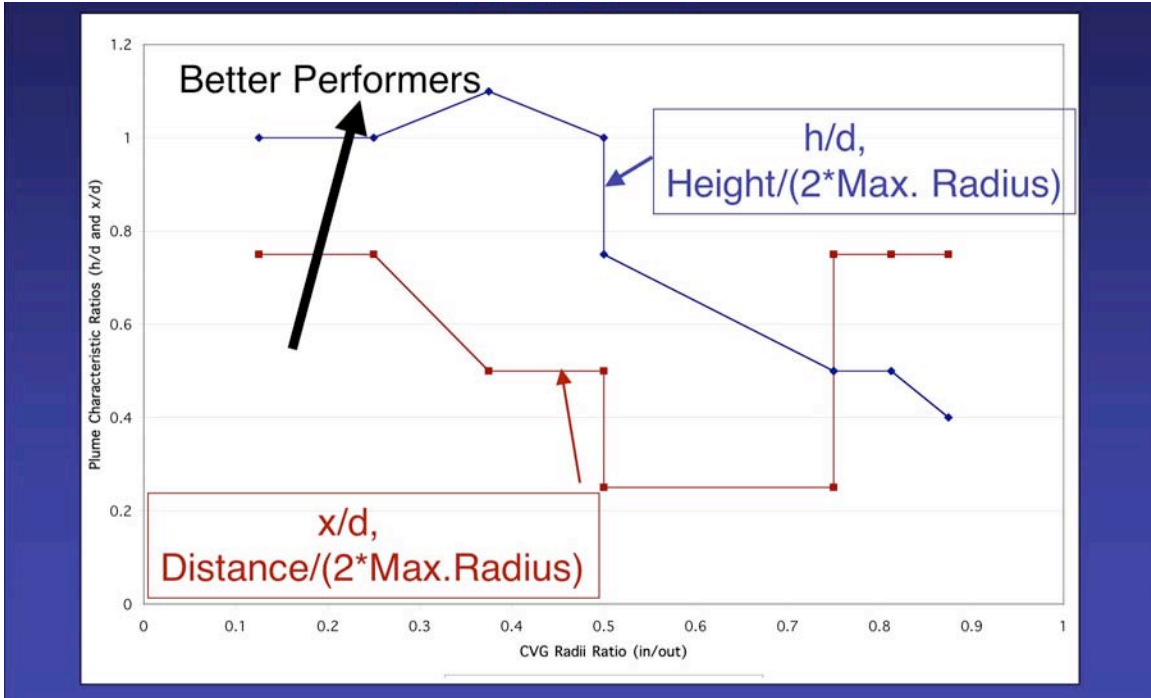


Figure 15. Plume performance of CVGs in LaRC SBRT.

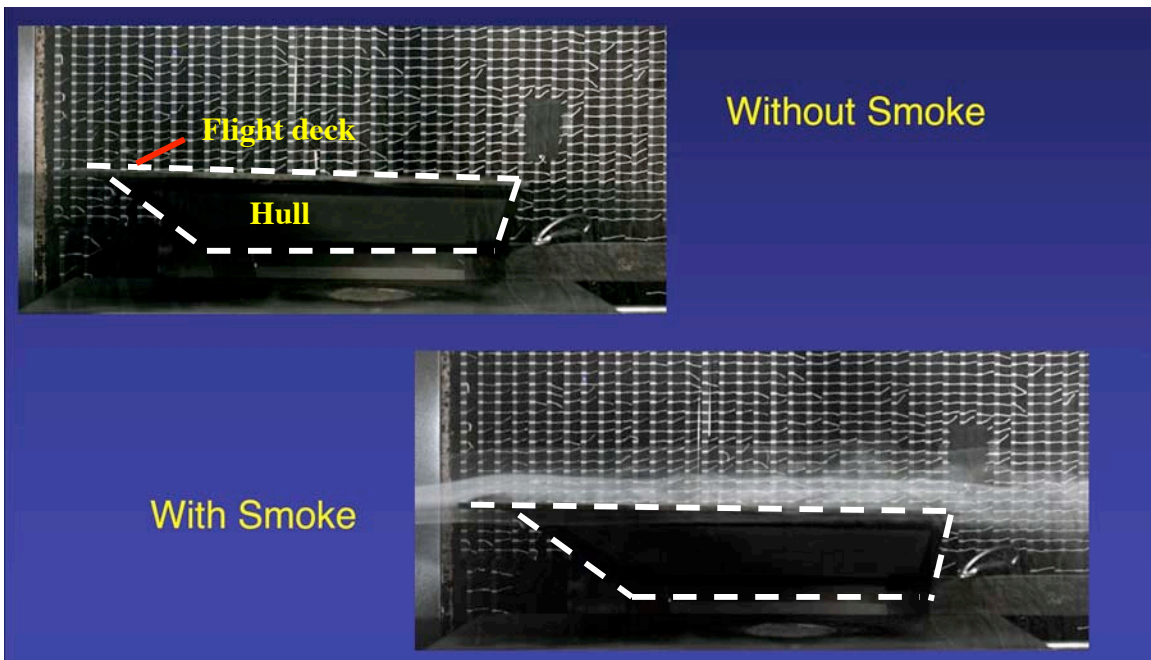


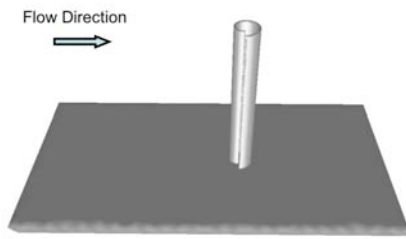
Figure 16. Portion of a helicopter carrier model representation (forward port-quarter) as viewed from the port-side in LaRC SBRT with and without smoke flow.



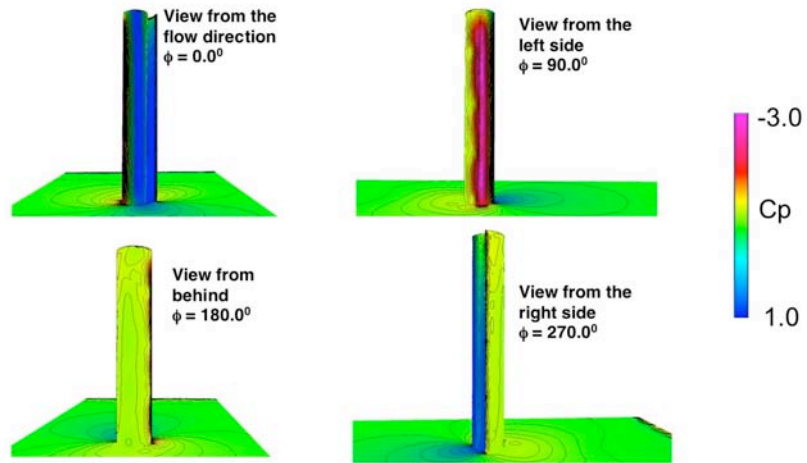
Figure 17. Aspect ratio 0.5 rectangular wing and flush mounted modified CVG device at AOA = -5°.



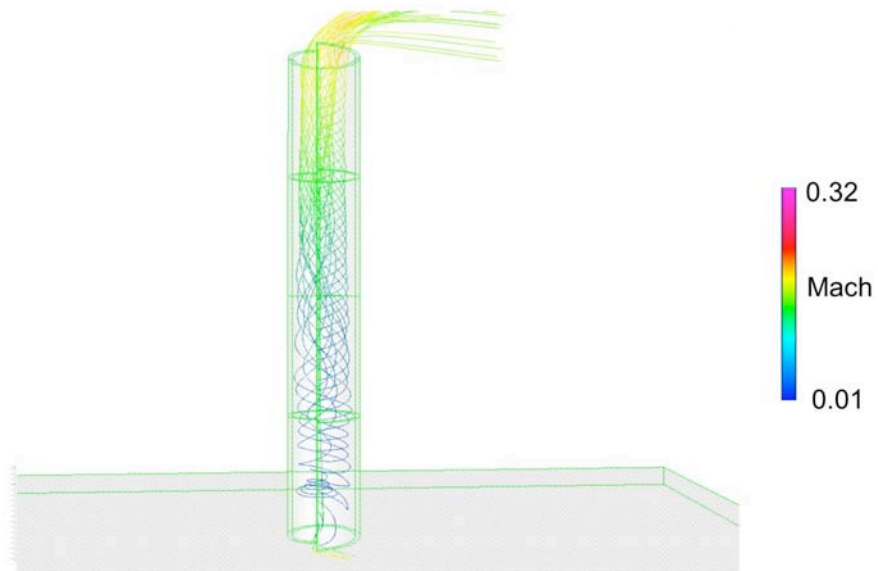
Figure 18. USM3D solution for modified CVG device mounted on flat plate at $\alpha \sim 0^\circ$ (looking aft): C_p results.



(a)



(b)



(c)

Figure 19. USM3D results for CVG on flat plate with gap = 0.5 inches, height = 10 inches, $M = 0.179$ and $R_n/ft = 1.27 \times 10^6$: (a) Geometry and orientation; (b) Surface pressures, (c) Mach number levels. (Results obtained by P. C. Parikh,)

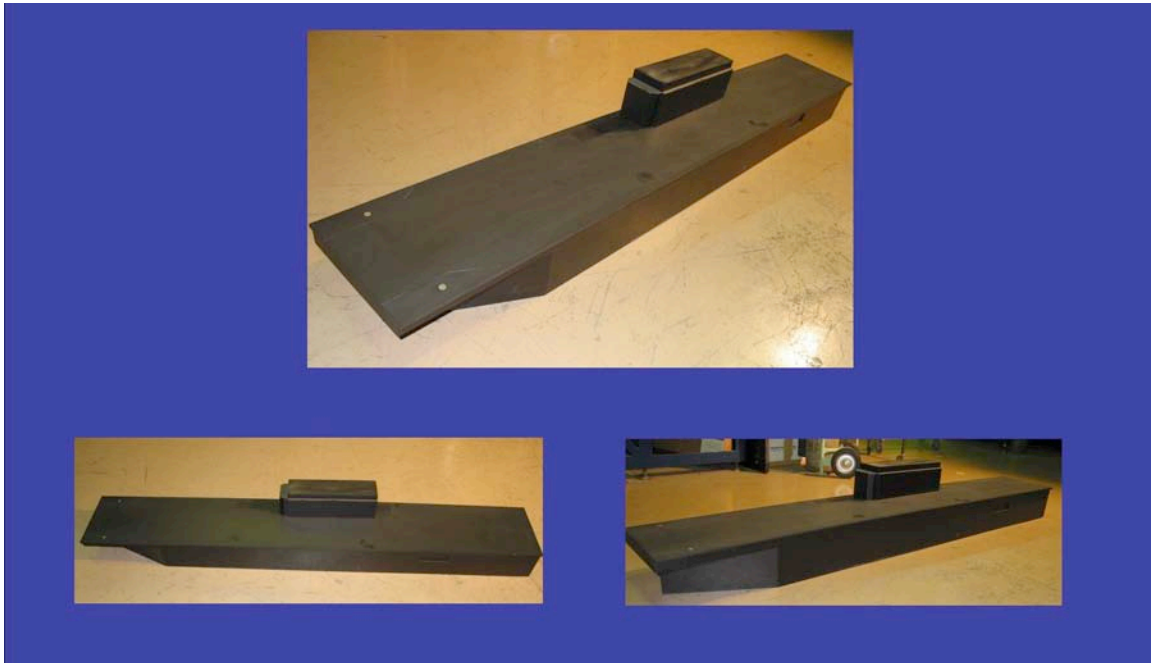


Figure 20. Simplified 1/120th scaled LHD carrier wind-tunnel model, as received on loan from Ms. Gloria Yamauchi of NASA Ames Research Center.



Figure 21. Simplified 1/120th scaled LHD carrier model with modified flight deck in 14ft by 22ft wind-tunnel.

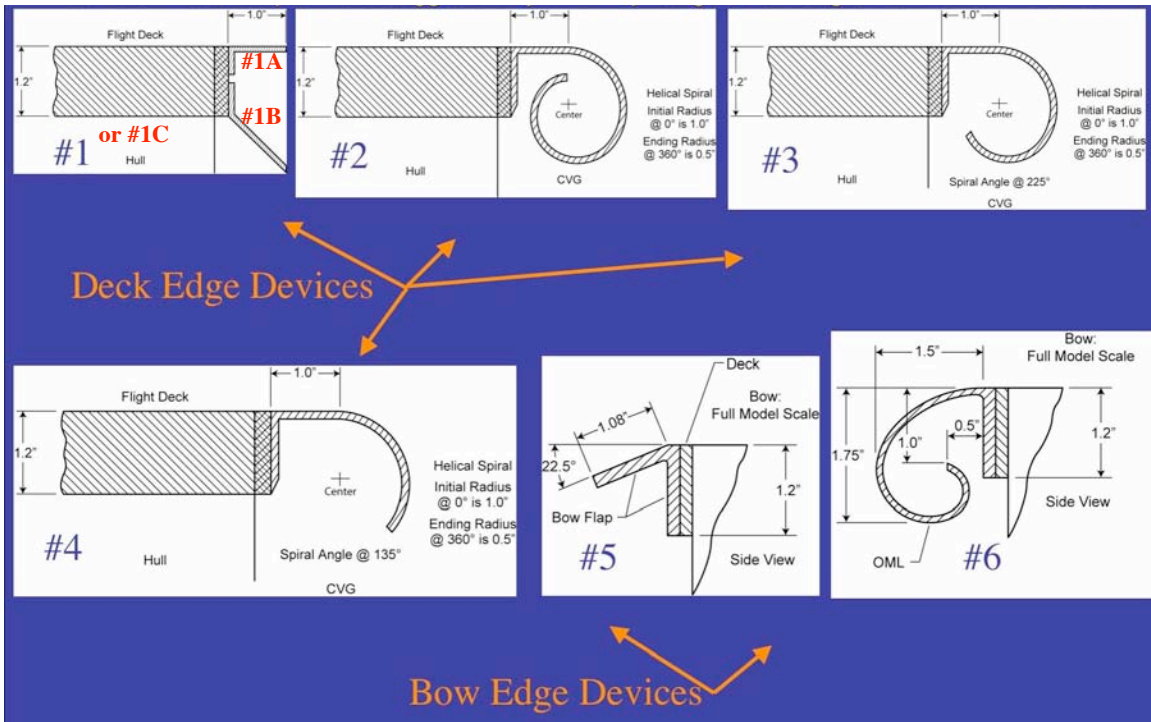


Figure 22. Sketches of NVFDs for LHD model. Note: Deck edge device #1 or #1C is the complete device as shown, whereas #1A is just the upper part and #1B is just the lower part. Some of the deck-edge shapes were suggested by Drs. Raj Nangia and Doug Greenwell of the U.K.

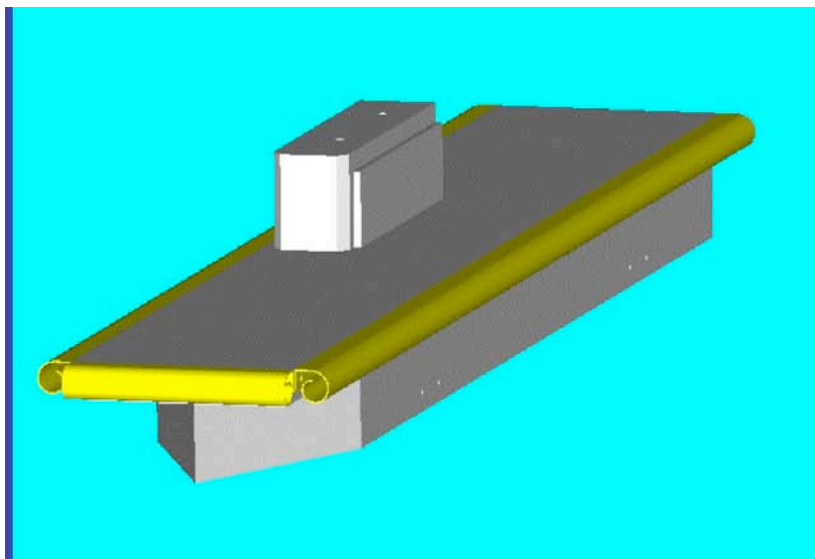
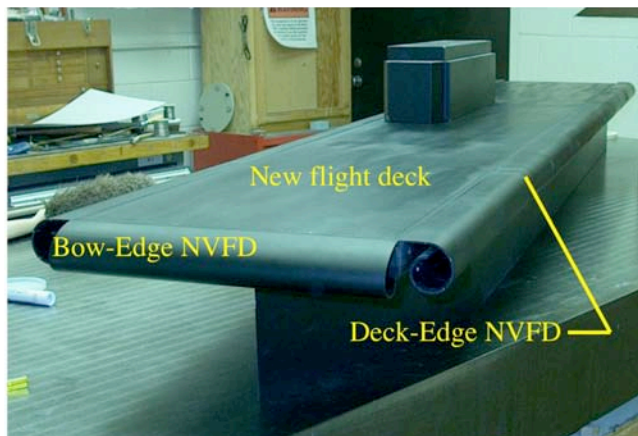


Figure 23. Isometric of CVGs applied to the simplified LHD carrier model.



(a)



(b)

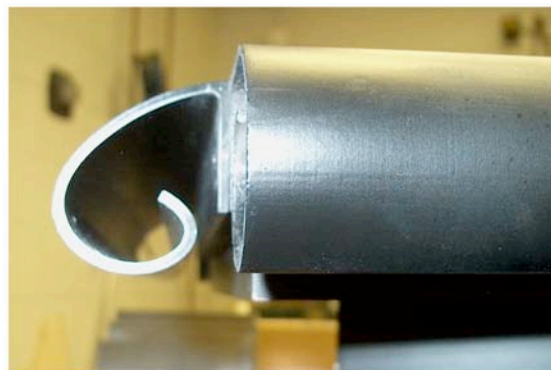


(c)

Figure 24. Three-quarter views of simplified LHD model with deck- and bow-edge NVFDs installed: (a) port, (b) starboard, and (c) stern.



Close-up of Port, Front-View of Deck NVFD #2



Close-up of Front, Port-View of Bow NVFD #6

Figure 25. Close-up views of deck (#2) - and bow-edge (#6A) NVFDs on LHD model.



Figure 26. Three views of simplified 1/120th scaled LHD model with devices in 14 ft by 22 ft wind-tunnel.

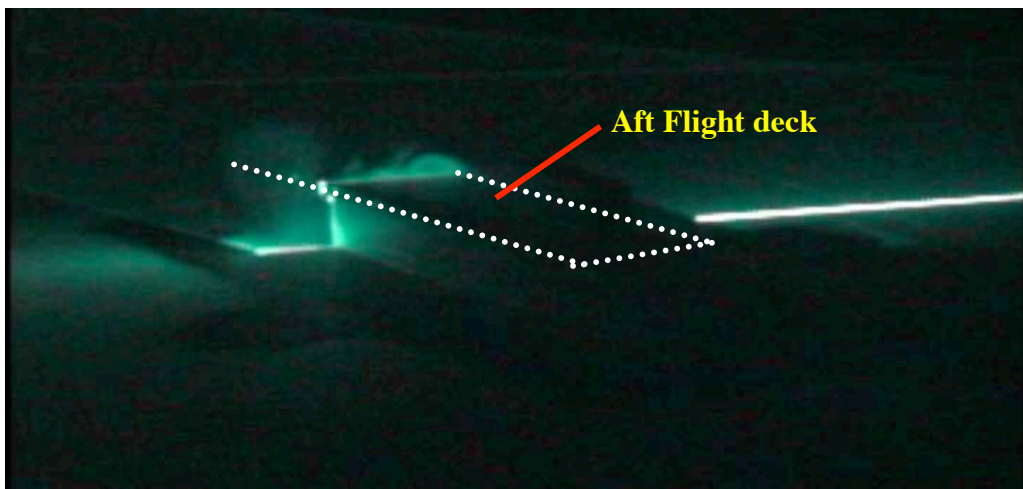


Figure 27. Simplified 1/120th scaled LHD model in 14 ft by 22 ft wind-tunnel at $\Psi = -30^\circ$; from video clip.

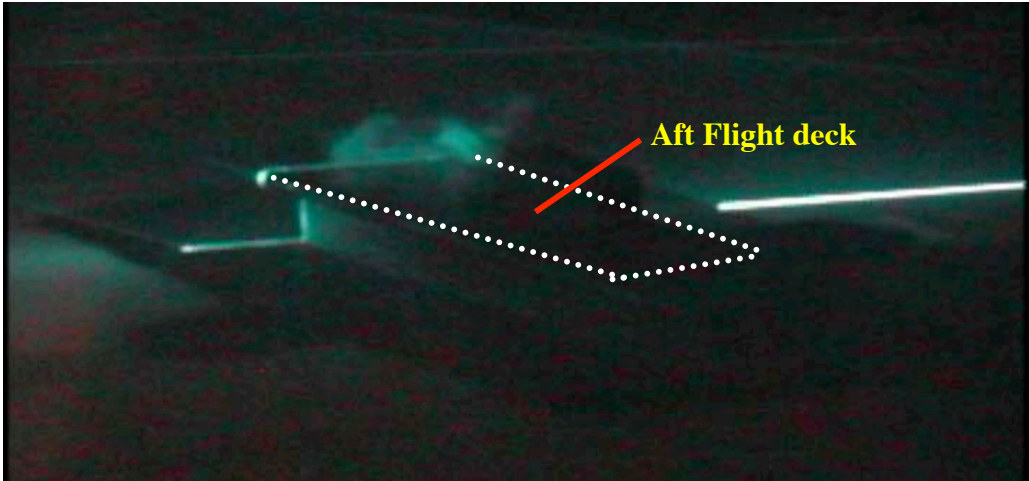
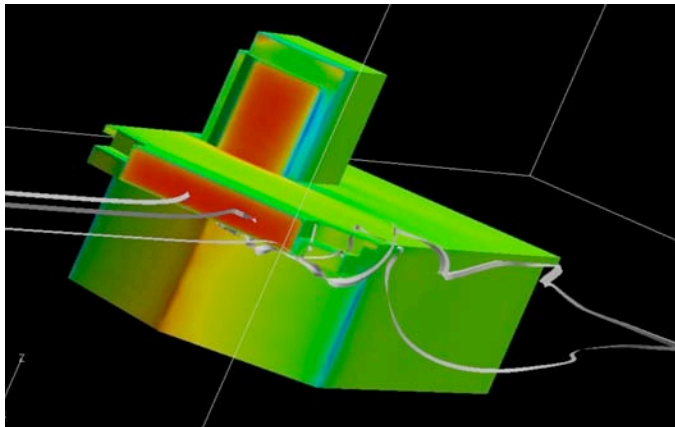
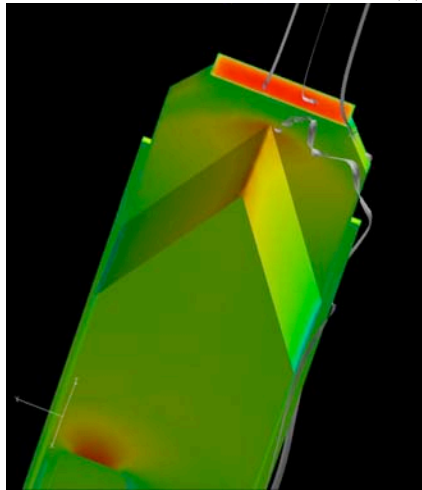


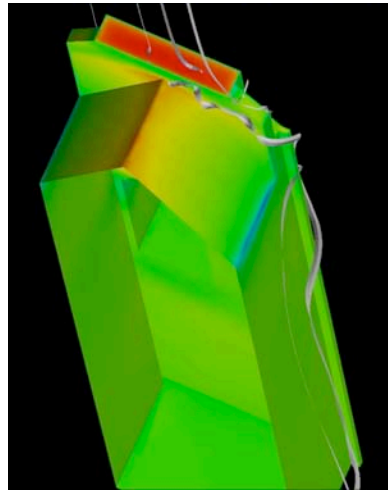
Figure 28. Simplified 1/120th scaled LHD model with Deck Edge device #2 and Bow Edge device #6A in 14 ft by 22 ft wind-tunnel at $\Psi=-30^\circ$ and at \sim same longitudinal location as for baseline; from video clip.



(a)

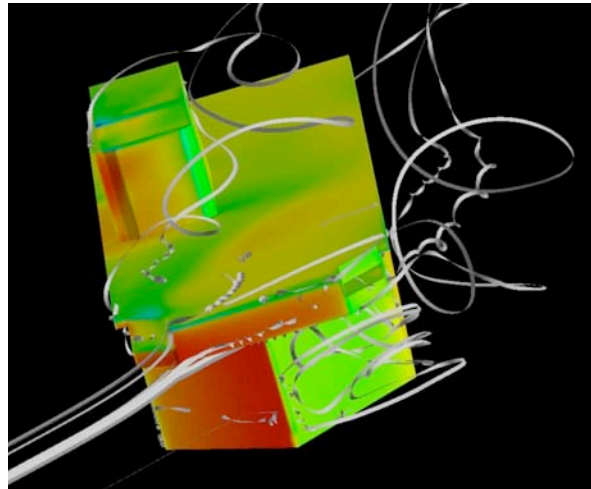


(b)

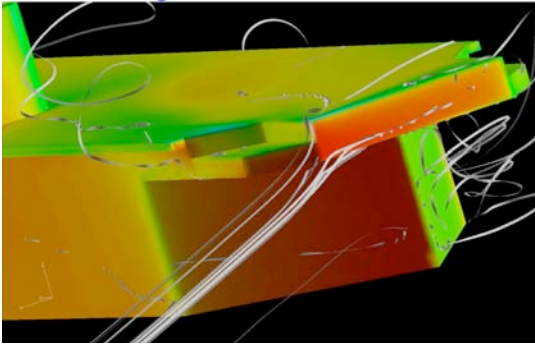


(c)

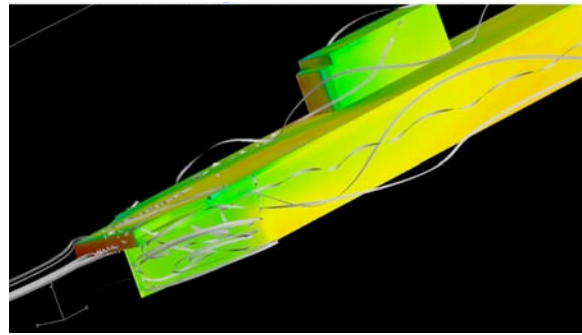
Figure 29. View of NAVAIR/COBALT streamlines for simplified LHA baseline model at $\Psi = 0^\circ$ from: (a) port, (b) bottom, (c) hull, port edge.



(a)

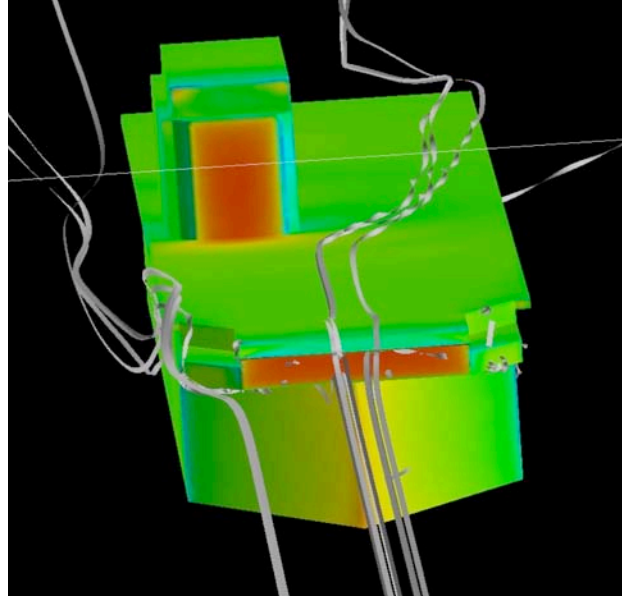


(b)

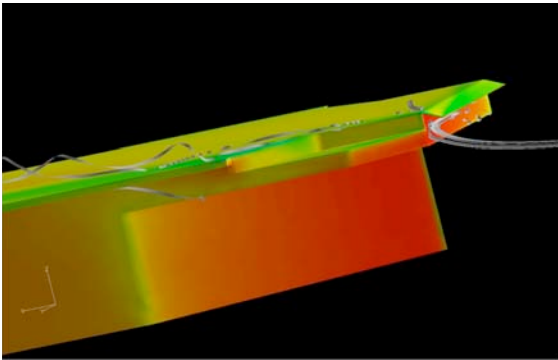


(c)

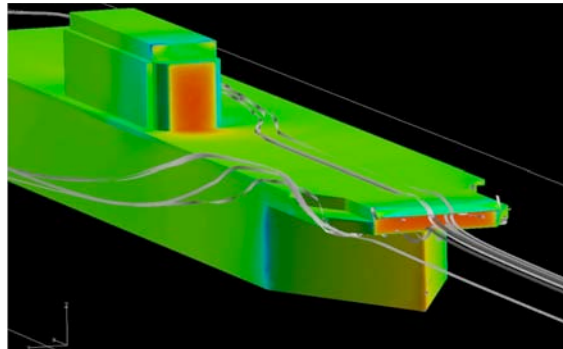
Figure 30. View of NAVAIR/COBALT streamlines for simplified LHA baseline model at $\Psi = 30^\circ$ from: (a) head-on, (b) starboard, (c) port.



(a)

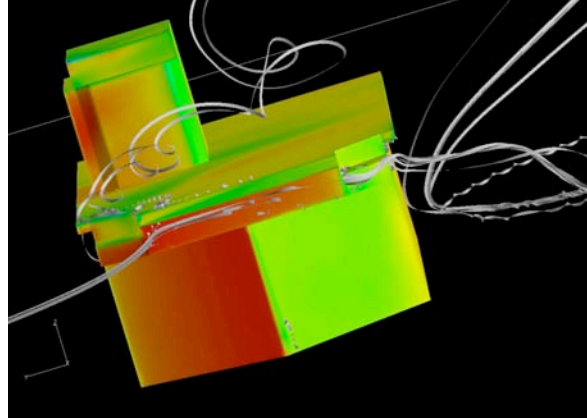


(b)

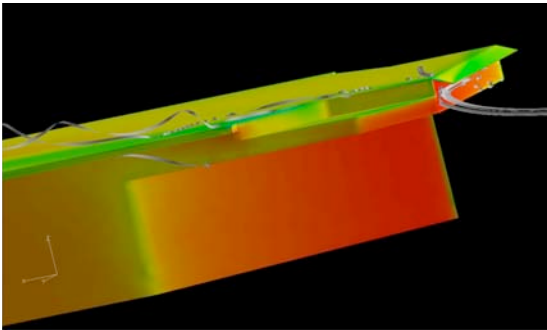


(c)

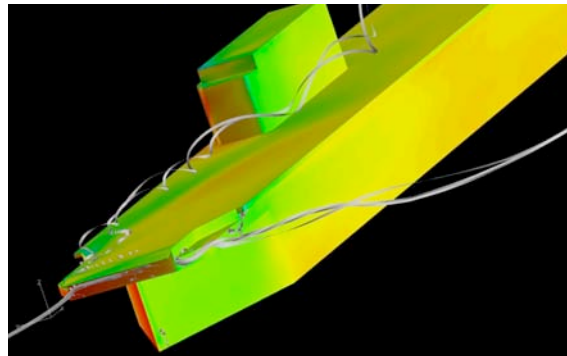
Figure 31. View of NAVAIR/COBALT streamlines for simplified LHA baseline model with bow-flap at $\Psi = 0^\circ$ from: (a) head-on, (b) starboard, (c) port.



(a)



(b)



(c)

Figure 32. View of NAVAIR/COBALT streamlines for simplified LHA baseline model with bow-flap at $\Psi = 30^\circ$ from: (a) head-on, (b) starboard, (c) port.

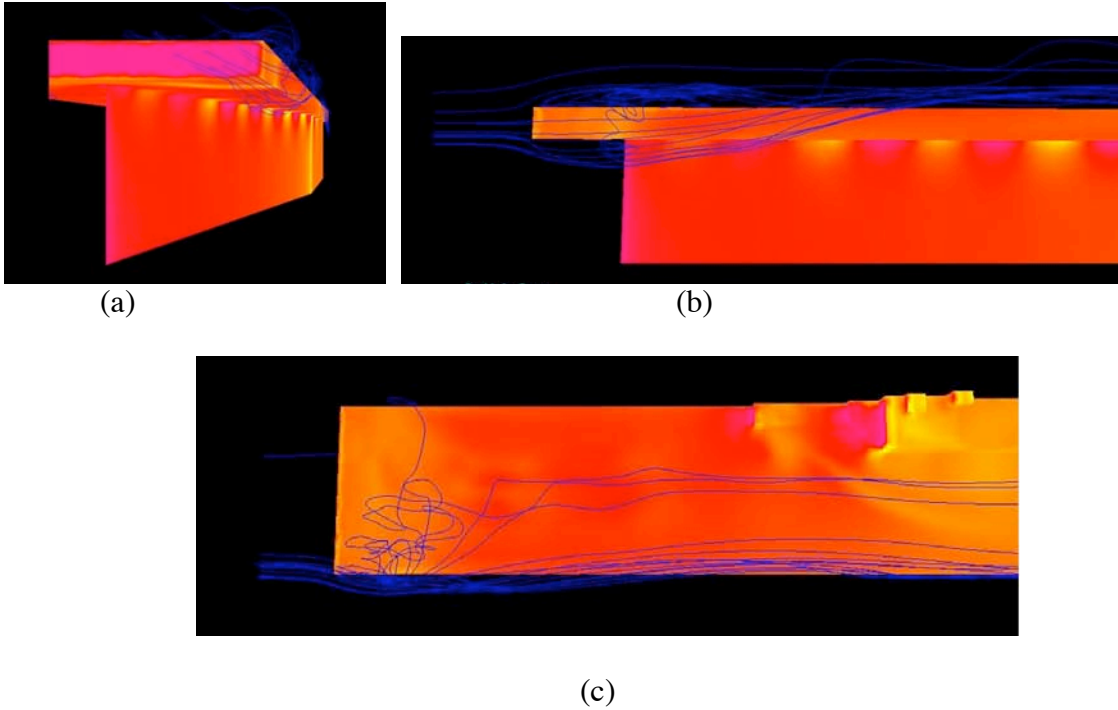


Figure 33. View of NASA/ODU-CEA/USM3D streamlines for simplified LHD baseline model at $\Psi = 0^\circ$ from: (a) head-on, (b) port, (c) top.

Manufacturer:	TSI
Camera:	PIVCAM 13-8, 1.3 Megapixel, 8 hz max, 12 bit resolution
Camera Interface:	TSI Laserpulse synchronizer, commercial frame grabber
Laser:	New Wave Y50-15 Dual YAG; 50 mJ/pulse, 15 pulses/sec max.
Seeding:	Mineral oil, ROSCOE fogger
Software:	TSI Insight
Host Computer:	Dell PC, dual processor, Windows OS
Max PIV rate (2D):	3.75 hz

Figure 34. PIV system characteristics as used in the ODU wind-tunnel.

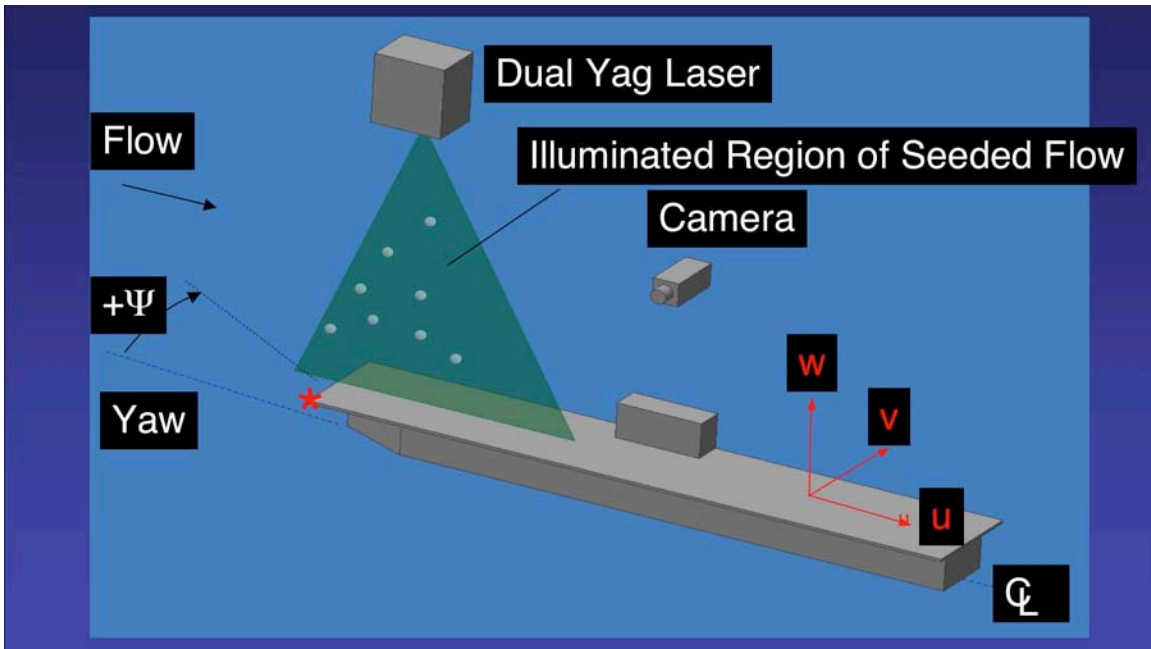
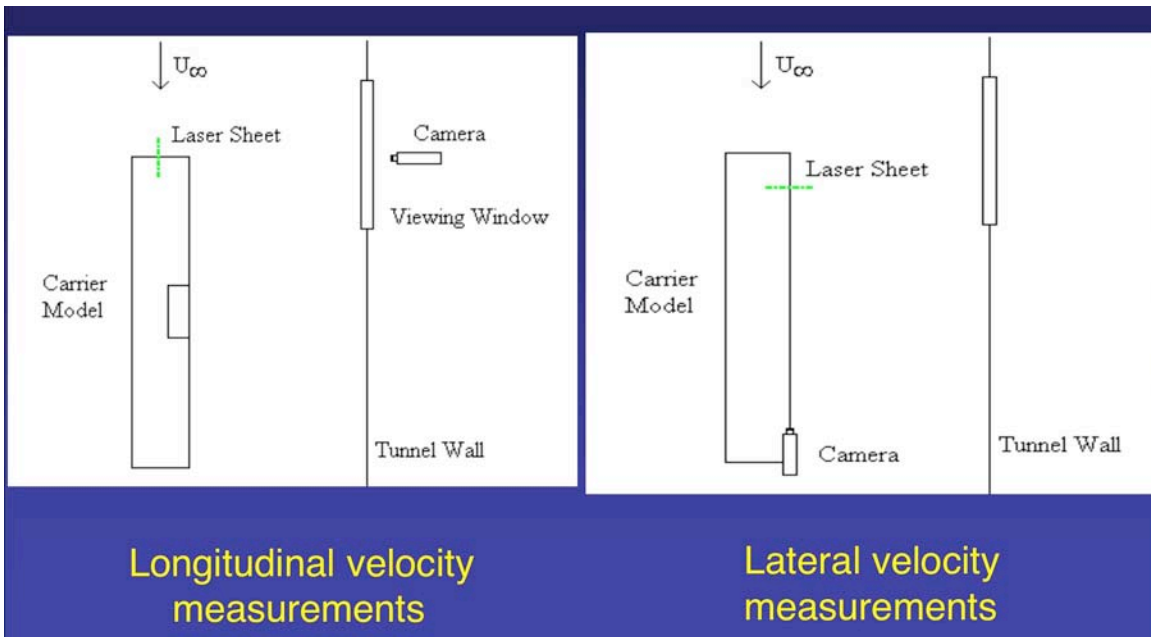


Figure 35. PIV system and model orientation in ODU wind-tunnel. * Represents point where corner flow originates that streams across flight deck when $\Psi > 0^\circ$.



Longitudinal velocity measurements

Lateral velocity measurements

Figure 36. PIV system and model orientation in ODU wind-tunnel.

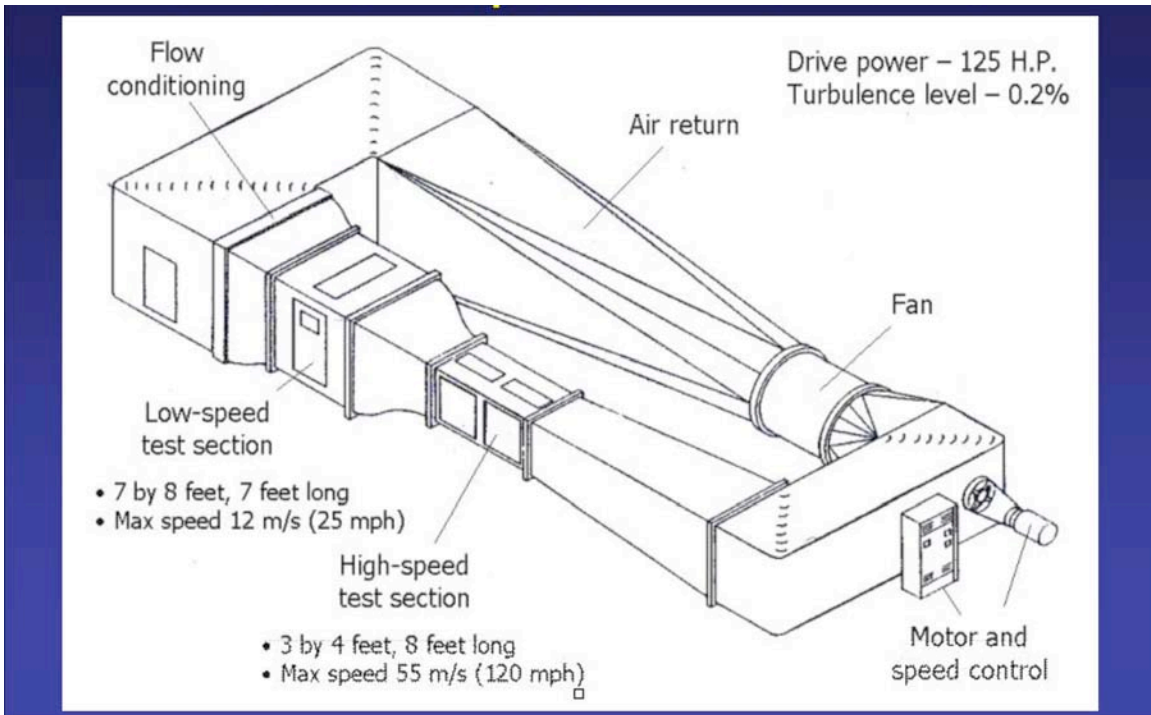


Figure 37. ODU low-speed wind-tunnel.



Figure 38. Carrier model in ODU wind-tunnel.

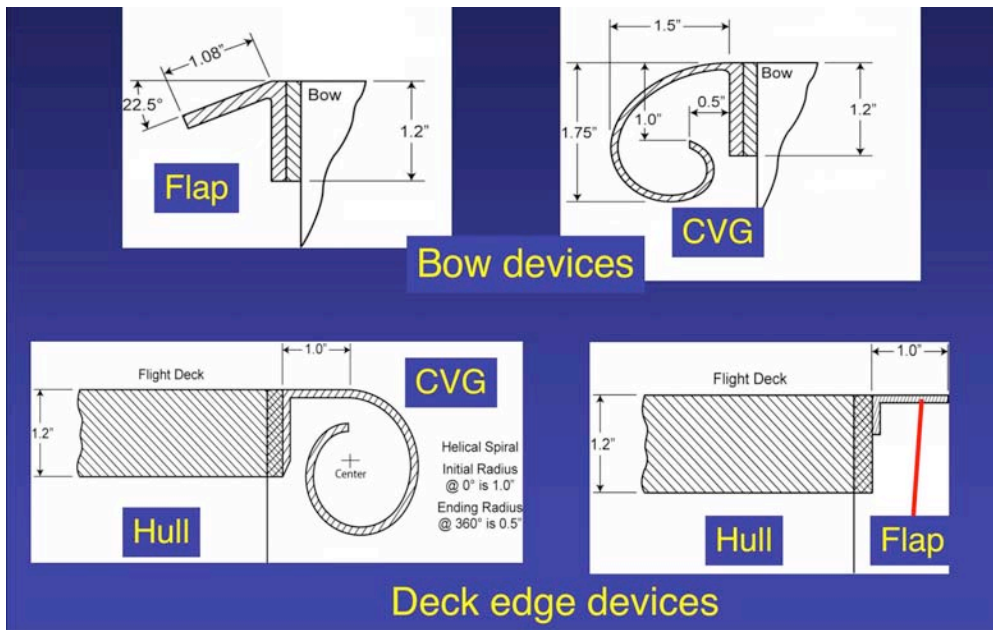


Figure 39. Bow and deck edge devices tested on carrier model in ODU low-speed wind-tunnel using PIV.

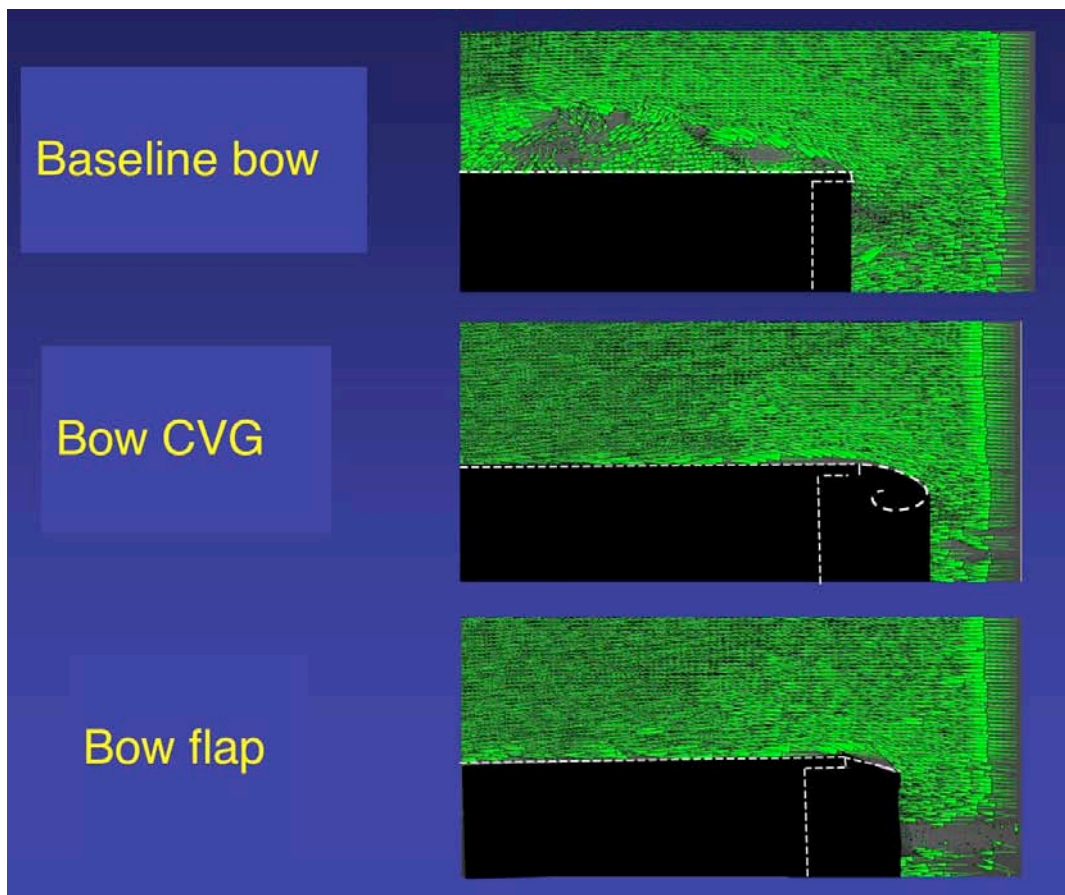


Figure 40. Centerline u-velocity vectors for three configurations at $\Psi = 0^\circ$ as viewed from side.

Figure 41
% Node Avg. Turbulence
Centerline
Yaw = 0 deg
Baseline Bow
Side View

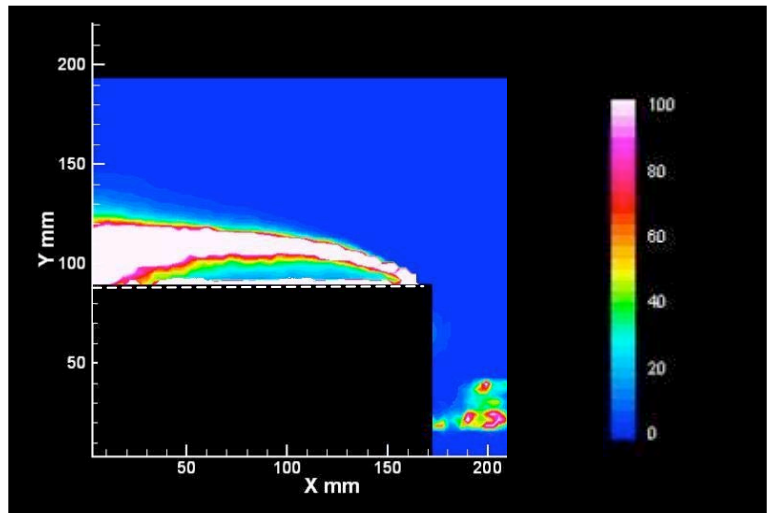


Figure 42
% Node Avg. Turbulence
Centerline
Yaw = 0 deg
Bow CVG
Side View

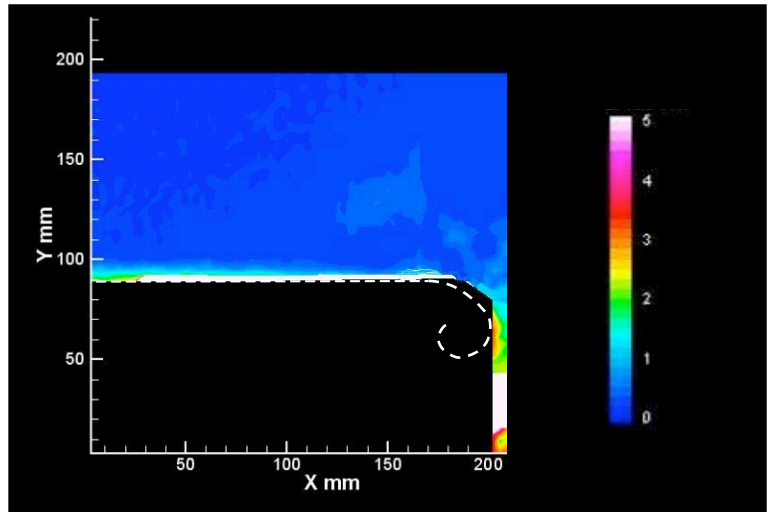


Figure 43
% Node Avg. Turbulence
Centerline
Yaw = 0 deg
Bow Flap
Side View

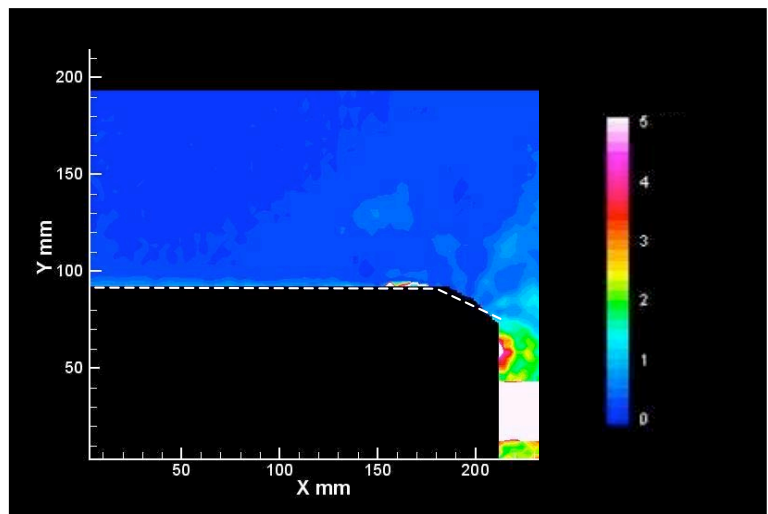


Figure 44
% Node Avg. Turbulence
Centerline
Yaw = 20 deg
Baseline Bow
Side View

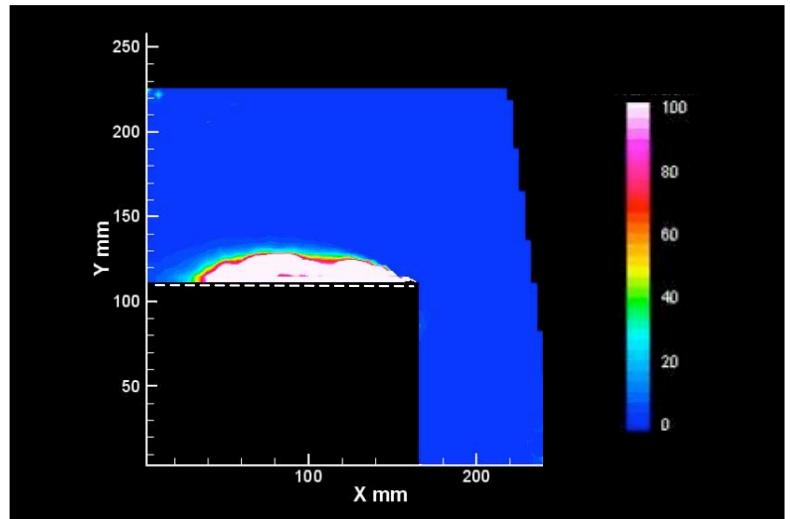


Figure 45
% Node Avg. Turbulence
Centerline
Yaw = 20 deg
Bow CVG
Side View

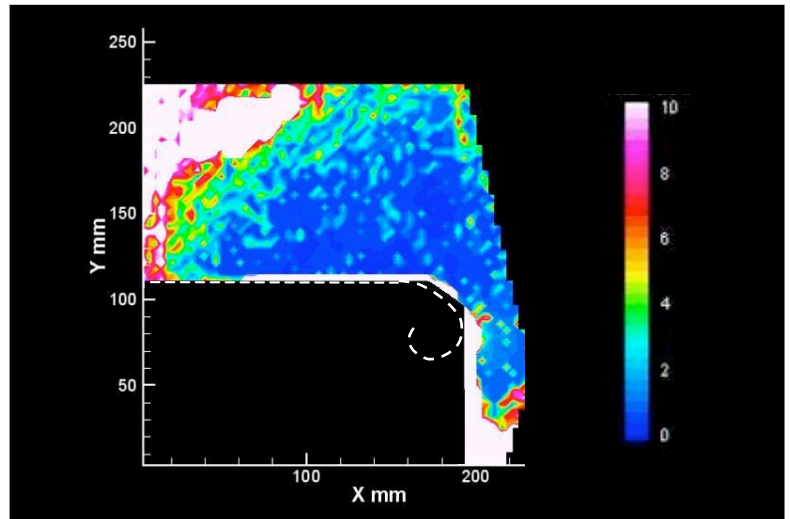


Figure 46
% Node Avg. Turbulence
Centerline
Yaw = 20 deg
Bow Flap
Side View

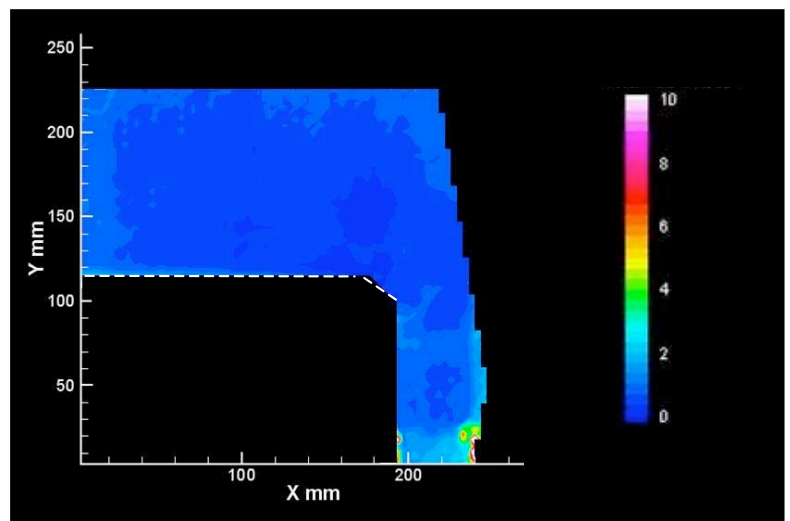


Figure 47
% Node Avg. Turbulence
Centerline
Yaw = 20 deg
Bow and Side CVG
Side View

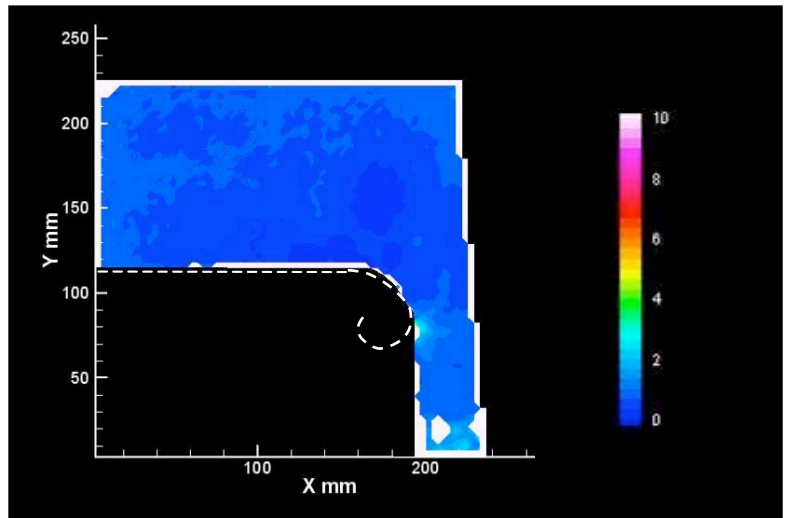


Figure 48
% Node Avg. Turbulence
Centerline
Yaw = 20 deg
Bow and Side Flap
Side View

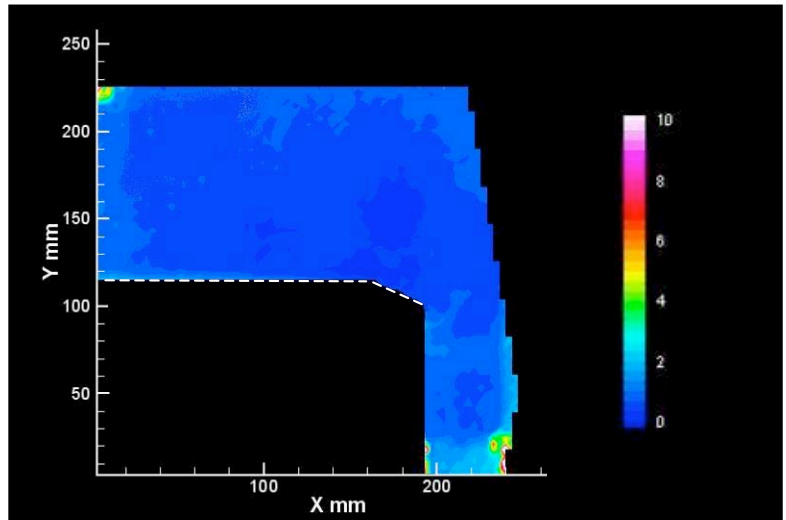


Figure 49
% Node Avg. Turbulence
Centerline
Yaw = 20 deg
Side CVG Only
Side View

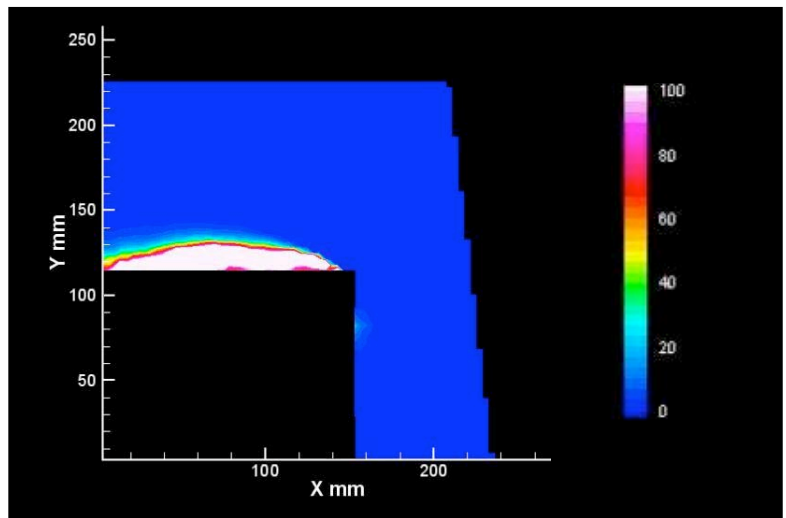


Figure 50
% Node Avg. Turbulence
Yaw = 20 deg
Baseline Bow
Rear View

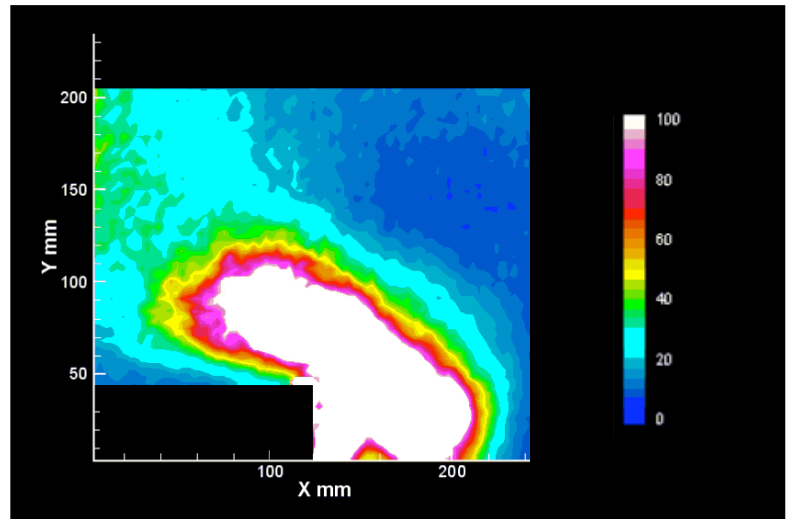


Figure 51
% Node Avg. Turbulence
Yaw = 20 deg
Bow CVG
Rear View

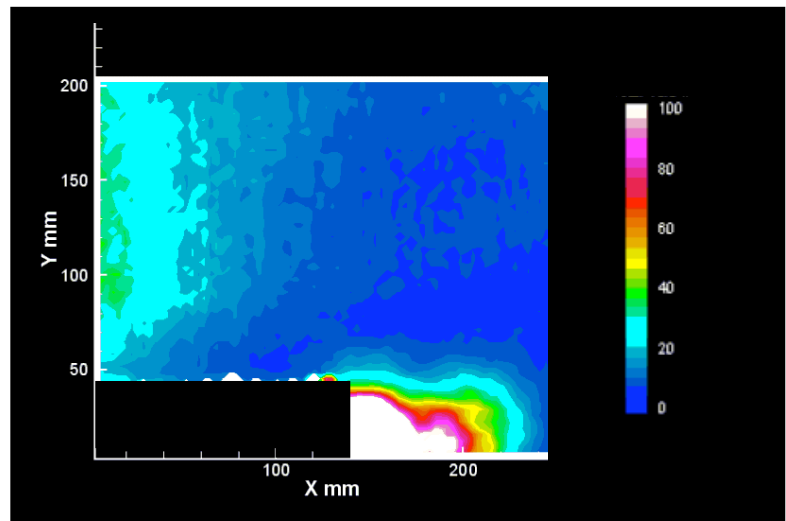


Figure 52
% Node Avg. Turbulence
Yaw = 20 deg
Bow Flap
Rear View

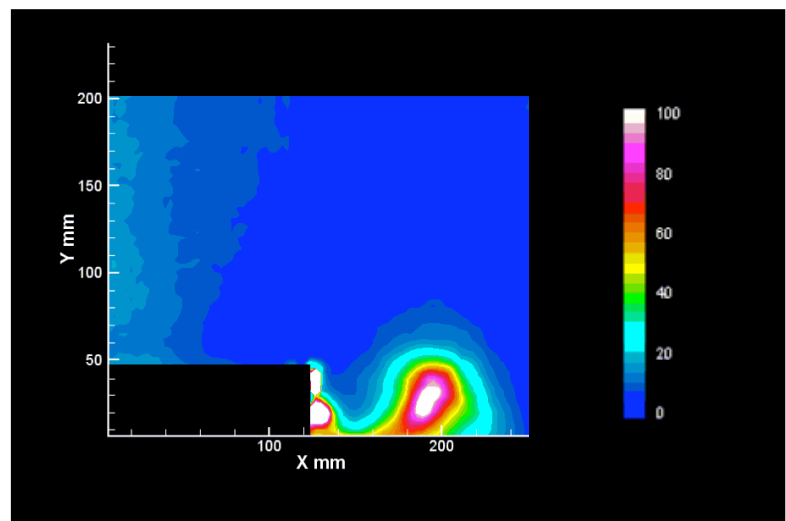


Figure 53
% Node Avg. Turbulence
Yaw = 20 deg
Bow and Side CVG
Rear View

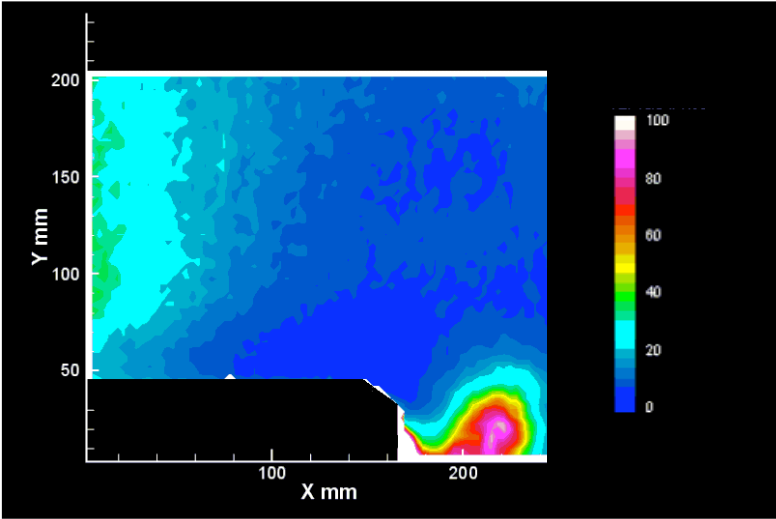


Figure 54
% Node Avg. Turbulence
Yaw = 20 deg
Bow and Side Flap
Rear View

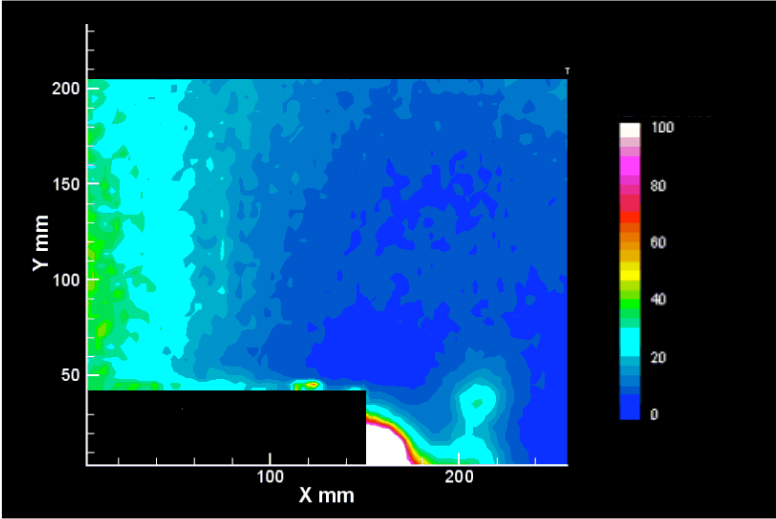


Figure 55
% Node Avg. Turbulence
Yaw = 20 deg
Side CVG only
Rear View

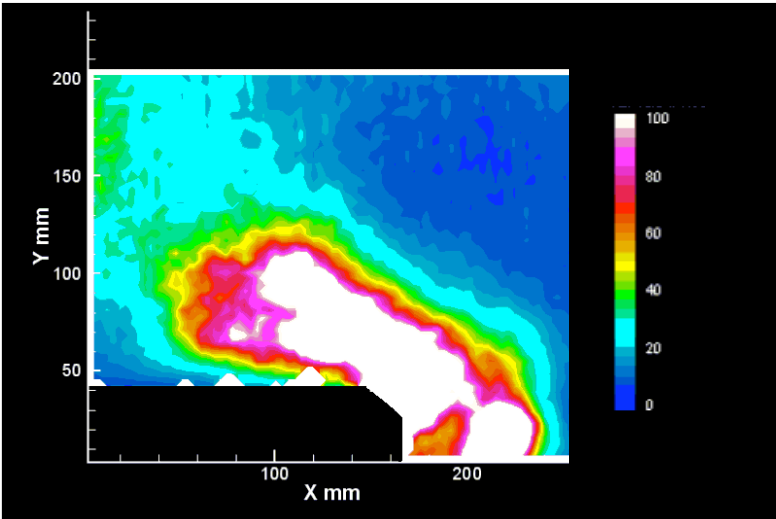


Figure 56
% Vorticity
Centerline
Yaw = 0 deg
Baseline Bow
Side View

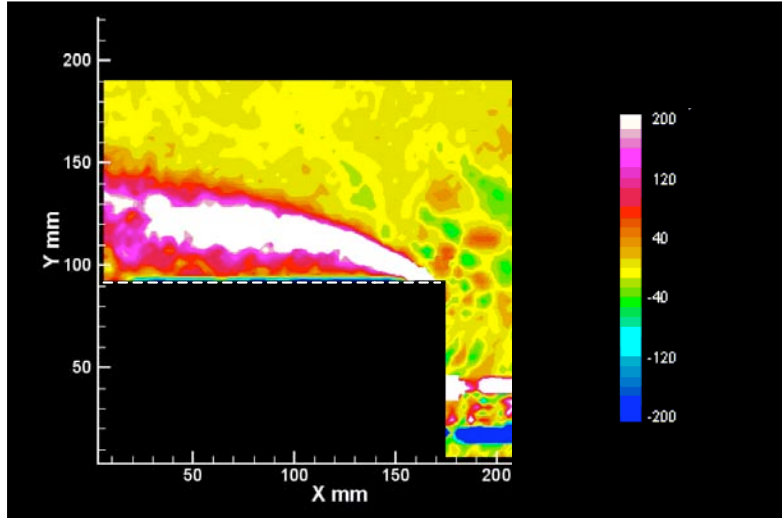


Figure 57
% Vorticity
Centerline
Yaw = 0 deg
Bow CVG
Side View

